minerals

MDPI

Article

Insights into the Weathering Crust Reservoirs of Granitoids: A Case Study from Qinghai Oilfield of Qaidam Basin, Northwest China

Xiaoqin Jiao [1,2,3], Huapeng Niu [1,2,*], Qingbin Xie [1,2], Massimiliano Zattin [3], Yongshu Zhang [4], Zhixiong Wu [4], Yuhe Chen [1,2], Xian Zhao [1,2], Shan Liu [1,2] and Xinhong Wei [1,2]

[1] State Key Laboratory of Petroleum Resource and Prospecting, China University of Petroleum, Beijing 102249, China
[2] College of Geosciences, China University of Petroleum, Beijing 102200, China
[3] Department of Geosciences, University of Padova, 35131 Padova, Italy
[4] Exploration and Development Institute of Qinghai Oilfield Company, PetroChina, Dunhuang 736202, China
* Correspondence: niuhuapeng@cup.edu.cn

Abstract: With proven reserves of 9.836×10^{10} m^3, the largest known natural gas reservoir among terrigenous basement rocks has been discovered within the granitoids of the northern Qaidam Basin. Due to their high heterogeneity, the genesis of basement reservoirs remains unknown. Herein, the structure of the weathering crust in granitoids and their potential controlling factors on the reservoir development mechanism are discussed using a multidisciplinary approach based on data from cores, thin sections, scanning electron microscopy (SEM), conventional and imaging logs, and physical property and major elements analyses. Moreover, the classification standard of the weathering crust structure is established. The dissolution belt holding diverse reservoir spaces accounts for more than 50% of the total porosity, while the disintegration belt is the main context for the development of cleavage fractures and crack fractures. The original pores exist mainly among the crystal grains of quartz and mica, while the secondary pores and fractures were generated by the alteration of aluminosilicate minerals as well as biotite or hornblende. The quality of these reservoirs is controlled by their mineral composition, tectonic uplift, faulting, and paleogeomorphology. The femic granitoid is the main reservoir-forming lithology in the case of dissolution, while the felsic granitoid is more likely to develop cracks. The formation of the disintegration belt is significantly linked to the presence of faulting. These belts were mostly induced by tectonic deformation along the Altyn fault belt from the late Oligocene to the early Miocene. The diversity in paleogeomorphology influences the extent of the weathering. The exhumation in the Altyn terrane from the late Jurassic to the Cenozoic corresponds to the weathering and hypergene leaching period of the weathering crust within granitoids. Three types of reservoirs are present in the rocks: fractured-porous (Type I); porous (Type II); and fractured (Type III). The fractured-porous and fractured reservoirs were developed mainly in the granitic gneiss and granite, while the porous reservoir was formed in granitic diorite and granitic gneiss. The reservoirs that developed in the weathering crust of granitoids are dominated by Type I and Type II. The highest quality reservoir, which is the fractured-porous type, developed mainly in the dissolution belt of the weathering crust, and has a porosity ranging from 1.56% to 8.48% and a permeability ranging from 0.03 mD to 14.48 mD. The mechanisms of the development of weathering crust reservoirs provide further information for the hydrocarbon exploration of basement rocks worldwide.

Keywords: basement reservoir; weathering crust; granitoid; hydrocarbon; Qaidam Basin

Citation: Jiao, X.; Niu, H.; Xie, Q.; Zattin, M.; Zhang, Y.; Wu, Z.; Chen, Y.; Zhao, X.; Liu, S.; Wei, X. Insights into the Weathering Crust Reservoirs of Granitoids: A Case Study from Qinghai Oilfield of Qaidam Basin, Northwest China. *Minerals* **2023**, *13*, 23. https://doi.org/10.3390/min13010023

Academic Editor: Georgia Pe-Piper

Received: 10 November 2022
Revised: 12 December 2022
Accepted: 17 December 2022
Published: 23 December 2022

1. Introduction

Basement rocks, a crucial type of reservoir, are characterized by typical features such as a strong physical heterogeneity, multiple tectonisms, and a deep burial [1,2]. Basement

rocks with abundant hydrocarbons have been extensively discovered [3–5]. The total proven reserves of basement reservoirs (including Bonger Basin, Suez Basin, Qaidam Basin, Panno Basin, and Tampico Basin) contribute approximately 15% of the world's known reserves [6]. The conventional production of petroleum from sedimentary rocks is currently occurring in increasingly tough conditions [7,8], thus making the exploration of unconventional reservoirs, such as basement reservoirs, urgent [2,9,10]. The basement rocks, especially metamorphics, carbonates and volcanics, have been broadly analyzed in terms of petrology, time–temperature evolution, and property appraisal [11–13]. As documented by Ma et al. [14], granitoids make up about 40% of basement rocks. In particular, as the igneous rocks have a higher effective porosity and permeability when compared with other basement rocks, the oil and gas exploited in granitoids contribute 75% of the total amount found in basement rocks [15]. Therefore, granitoids are crucial targets for basement reservoir appraisal and have a great potential for future energy exploration [16].

Natural fracturing is a key parameter in granitoids, and the prediction of fracture distribution can be made using seismic, wireline, numerical simulation, and core data [9,17–19]. Some granitic reservoirs rich in hydrocarbons, however, are dominated not only by fractures but also by pores [20]. The pores and fractures developed within basement rocks are usually located at the topographical highs or in the inner parts of the weathering crust [21]. The basement reservoirs are thus dominated by secondary pores and fractures, which typically make the granitoids highly heterogeneous [22]. These basement reservoirs are eligible to be classified as fracture–pore-dominated and fracture-controlled types [15,23]. The reservoir spaces developed in granitoids are adjacent to the top of the weathering crust. Thus, far little attention has been given to the formation mechanism of different types of granitoid reservoirs. Furthermore, the contribution that diverse reservoir spaces have to the overall reservoir properties is still unclear [6].

Geophysical tools such as three-dimensional modeling has been widely used to study the controlling factors for oil and gas accumulation [4,13,24]. The hydrocarbon reservoirs formed in volcanic weathering crusts are now at the frontier of reservoir research [25,26]. Despite this, only a few volcanic hydrocarbon reservoirs have been found in or below Paleozoic strata, with the majority of the studies mainly focusing on lithology and chronology [27,28]. Amongst the known Paleozoic basements, the Qaidam Basin (northwestern China) is a promising target due to the development potential of weathering crust reservoirs in granitoids [29,30]. In 2012, large natural gas reserves were discovered in the Dongping area, where reservoirs consist mainly of granites and granitic gneiss [23]. By 2016, the defined geological reserves were equivalent to 10.2×10^8 t after the discovery of a further 29 oil and gas fields [29]. By 2017, the proven reserves of natural gas in the Jianbei area and the Dongping area reached 476.21×10^8 m^3 and 519.41×10^8 m^3, respectively. Significant exploration work has been conducted in the north Qaidam Basin and the areas of Niudong, Niuzhong, and Jianbei, where a daily capacity of 0.035×10^8 m^3 for natural gas in granitoids has been found. The Qaidam Basin hereby can represent an ideal case for exploring the genesis of weathering crust reservoirs and the significance of its influence on reservoir properties.

The characterization of weathering crusts has been broadly undertaken using petrographical factors, chemical indices, and engineering parameters [31–36]. Krauskopf [37] used the concentrations of immobile elements in parent rock to study chemical changes during weathering. The evaluation of the cation packing index and the cation exchange capacity were taken as an effective way to classify the degree of weathering [38–40]. Von Eynatten et al. [41] focused on the modeling of compositional changes in the weathering rocks. Typical properties used for the classification of weathering materials are the degree of mineral alteration, the presence of original texture, and the extent of weathering along joint planes [42,43]. Hence, the current quantitative classification system is predominantly related to the petrography and geochemistry of weathered outcrops, and there is a lack of evidence from the wireline log information to support the weathering classification. Parameters including the weathering potential index (WIP), residual value (V), chemical

index of alteration (CIA), chemical index of weathering (CIW), and paleoweathering index of alteration (PIA) are currently used to quantify the degree of weathering [40,44–48], but limited focus has been put on the classification of the structure of the weathering crust. The aim of this work is to elucidate the characterization of the weathering crust in granitoids and summarize their influence on the basement reservoir through in-depth experiments. Taking the Qinghai oilfield as an example, this study firstly employs the dataset based on the outcrop and the wireline logs. This dataset is a combination of cores, thin sections, scanning electron microscopy (SEM), conventional and imaging logs, physical properties, and major elements. These are used to classify the structure of the weathering crust, in order to understand the development mechanism and potential controlling factors of the weathering crust reservoir. This study therefore provides not only a significant supplement to the understanding of the weathering crust reservoir, but also crucial guidance to hydrocarbon exploration activities in basement rocks worldwide.

2. Geological Setting

The Qaidam Basin is a continental basin bounded by the Altyn strike-slip fault range to the north, the Qilian Mountain system to the northeast and the Kunlun Mountain belts to the southwest [49–51]. The formation of the basement of the Qaidam Basin involved tectono-thermal episodes, including Neoproterozoic, early Paleozoic, late Paleozoic, and Mesozoic [52]. The Mesozoic strata of the Qaidam Basin includes Jurassic and Cretaceous continental sediments, which are mainly composed of sandstone and conglomerate from fluvial to lacustrine depositional environments. The Cretaceous strata, meanwhile, were fully eroded in the sub-basins along the Altyn strike-slip fault [53] (Figures 1 and 2). The north Qaidam Basin along the Altyn strike-slip fault consists mainly of Proterozoic and Paleozoic basements, most of which were overlain by Paleozoic–Cenozoic sediments and intruded by Paleozoic granitoids [54–56]. Based on the chrono-stratigraphy and lithology, the strata of the study area are classically divided into lithostratigraphic units as follows: the crystalline basement (Proterozoic and Paleozoic), the Dameigou Formation (J_{1+2}d), the Lulehe Formation (E_{1+2}l), the lower member of the Xiaganchaigou Formation (E_3^1xg), the upper member of the Xiaganchaigou Formation (E_3^2xg), the Shangganchaigou Formation (N_1sg), the Xiayoushashan Formation (N_2^1xy), the Shangyoushashan Formation (N_2^2sy), the Shizigou Formation (N_2^3s), and the Qigequan Formation (Q_1q).

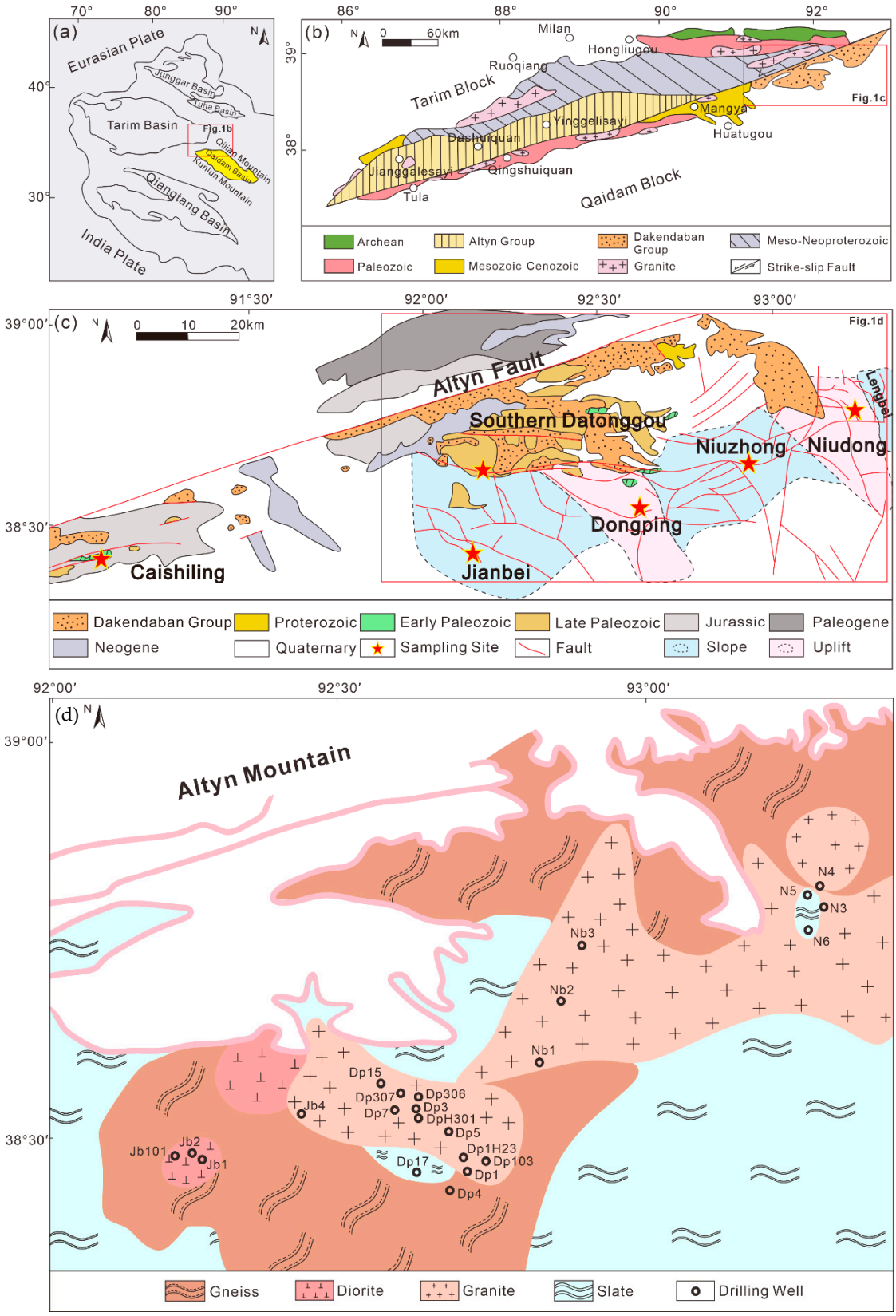

Figure 1. (**a**) Geological sketch map of the Qaidam region. (**b**) Tectonic sketch map of the Altyn orogenic belt (modified after Wu et al. [57] and Niu et al. [58]). (**c**) Sampled areas analyzed in this study (modified after Niu et al. [58]). (**d**) Lithological distribution and the drilling well locations of Qinghai oilfield in Qaidam Basin.

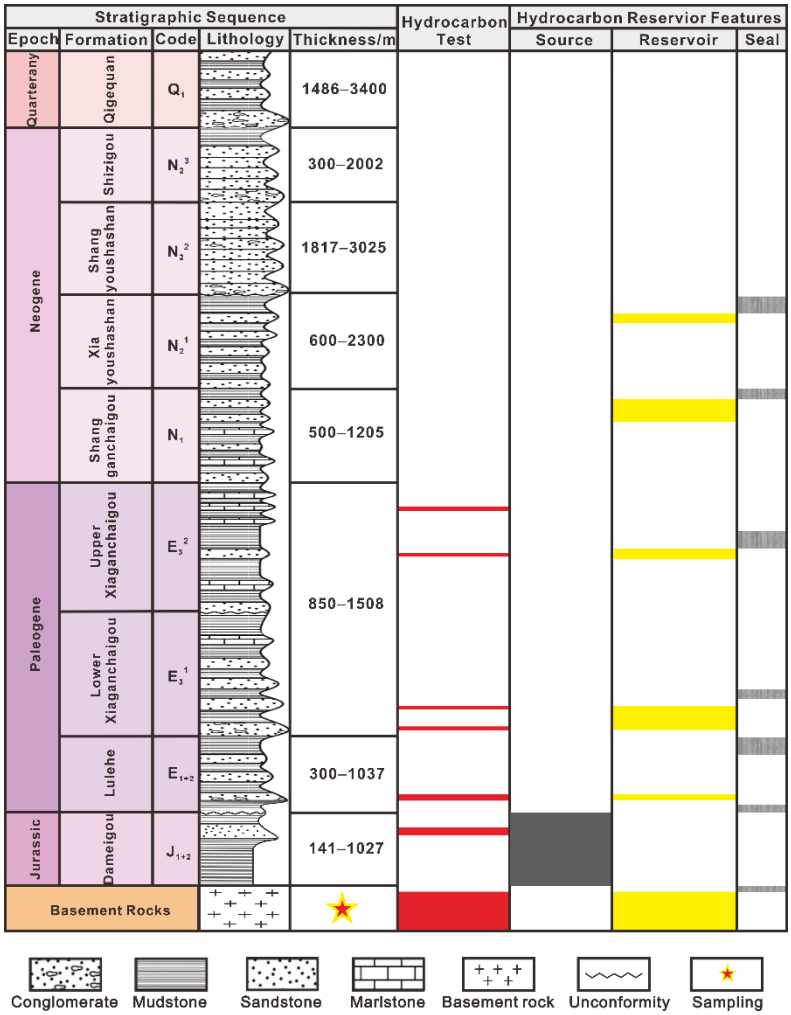

Figure 2. Stratigraphic column and distribution of source, reservoir, and seal rocks in Qaidam Basin (modified after Cheng et al. [59]; the hydrocarbon dataset is from PetroChina Qinghai oilfield).

Due to several collisional tectonic episodes which occurred during the Caledonian, Yanshanian, and Himalayan orogenic periods [60], structural units that include the Jianbei Slope, Dongping Uplift, Niuzhong Slope, Niudong Uplift, and Lengbei Slope were formed in front of the Altyn Fault (Figure 1). The Altyn Block experienced a Proterozoic orogeny firstly due to the continental collision and the postcollisional extension that occurred between the Tarim Basin and the Qaidam Basin. The formation stage of the Altyn Block was accompanied by multiple evolutions of ocean basins, island oceans, and paleocontinents in north Qaidam [56]. The paleo-ocean basins in the Altyn Block displayed extensional environments during the Cambrian and then developed collisional tectonics under the influence of the Caledonian orogenic event [61,62]. In conjunction with the subduction and reopening of the Paleo-Tethys Ocean in the south and the Paleo Asian Ocean in the north, from the Cambrian to the Permian, the Altyn Block has recorded not only several episodes of collisional tectonics but also the transition from continental collision to a postcollisional and extensional environment with the emplacement of magmatic rocks [50,56,57,61–64]. Approaching the Triassic, the southern segment of Gondwana started to break and expand [60], making the Qaidam Basin a rift basin in the early Jurassic until the early Cretaceous when it became contractional [53]. When the Yanshanian and Himalayan orogenic phases occurred in the Mesozoic and the Cenozoic, the India Plate experienced a northward subduction and collided with the Eurasian Plate, after which the Tethys Ocean underwent subduction and closure. The far-field effects of this tectonic movement included the formation of the Altyn strike-slip fault zone [65,66].

The outcropping sediments of the tectonic units situated in front of the Altyn fault zone are composed mainly of Jurassic, Paleogene, Neogene, and Quaternary strata (Figure 1). Further north, the basements that include granite, diorite, monzonite, syenite, and basaltic tuff were intruded by the Datonggou and Caishiling plutons [57,58].

With production reaching 519.41 $\times$ 10^8 m^3, the Dongping area has been shown to yield abundant natural gas from granitoids. The natural gas from granitoid reserves in the Jianbei area amount to 476.21 $\times$ 10^8 m^3. The Niuzhong and Niudong areas are dominated by basement reservoirs where about 800 m^3 per day of natural gas have been produced. The granites and granitic gneiss of this region are typically buried at a depth of 2000 m to 3000 m, and the Jurassic hydrocarbon source rocks are located in the northern margin of Qaidam Basin [67]. The Lower-Middle Jurassic strata are the main coal-bearing layers and the possible secondary hydrocarbon source rocks in the Qaidam Basin [53]. Deep fractures formed after tectonic events had transported the hydrocarbons from the generation sag to rock reservoirs [68].

3. Materials and Methods

This study employed data collected from 24 wells and 2 field outcrops which included: 5 wells from the Jianbei Slope (Jb1, Jb2, Jb4, Jb101, Jb1.1), 14 wells from the Dongping Uplift (Dp1, Dp3, Dp4, Dp5, Dp7, Dp103, Dp105, Dp106, DpH101, Dp306, Dp307, DpH301, Dp123, Dp1H23), 3 wells from the Niuzhong Slope (Nb1, Nb2, Nb3), 2 wells from the Niudong Uplift (N3, N4), and 2 outcrops (DT, CSL) from South Datonggou (38°37′42″ N, 92°12′07″ E) and Caishiling (38°23′19″ N, 90°31′59″ E), respectively. A series of analytical techniques including an optical microscopy observation, an SEM observation, wireline log data interpretation, a physical property analysis, and a geochemical data analysis were undertaken (Table 1).

Table 1. Summary of the dataset from the Qaidam Basin in this study.

Data	Thin Sections	SEM	Physical Property	Wireline Log	Major Eelements
Number	235	9	123	19	26
Depth/m	975.82–4945.87, outcrop	998.20–4645.90, outcrop	1879.80–3744.17	670–4750	1881.60–4645.90, outcrop

Petrography and reservoir property analyses were undertaken at China University of Petroleum-Beijing. Stained thin sections were made to gain textural and mineralogical information on different structures of the weathering crust. A petrographic analysis was undertaken using a Leica microscope under plane- and cross-polarized light, with 400-point mineral counts per section. At 95% confidence limits, the constituent which has an absolute error of about ±5% accounts for 50% of the sample [69]. In addition, polished sections were prepared and impregnated with blue-dyed resin to allow the identification of pore spaces and fractures. The SEM system employed in this study was a Quants 200F SEM coupled with X-ray energy dispersive spectroscopy, running at an accelerating voltage of 5 or 15 KV. A total of 123 borehole samples were tested for physical properties using a helium porosimeter and a gas permeameter by PetroChina Qinghai oilfield. The porosity testing was processed using an Ultra-pore^{TM} 400 porosimeter (Core Laboratories, Tulsa, OK, USA). The porosity was obtained after the volumes of grains and rocks were analyzed. The permeability was tested with an DX-07G permeameter (China Petroleum Exploration and Development Research Institute, Huiao Instrument Equipment Manufacturing Co., Ltd., Wuxi, China) based on Darcy's law. A total of 38 samples that were abundant in pores and fractures were selected to analyze their surface porosity.

The conventional modern wireline log data of 19 wells were collected from the PetroChina Qinghai oilfield, which comprised borehole-compensated sonic (AC), gamma ray (GR), bulk density (DEN), compensated neutron (CNL), and resistivity logs (RLLD and RLLS). The wireline log data were compiled using the Eclips-5700 logging series. Fullbore Formation MicroImager (FMI, Baker Atlas, Houston, TX, USA) logs were collected from the

19 wells mentioned above, which are widely used for structural characterization [70,71]. In the image logs, the open fractures display as dark, continuous or discontinuous sinusoidal waves, with a vertical resolution of 5 mm [72,73].

To define the chemical characteristics of the weathering crust, 18 borehole samples and 8 outcrop samples were chosen and analyzed at the laboratory of Wuhan Geosciences Institute in Hubei, China, including Jb1-1, Jb1-2 in the Jianbei area, Dp5-1, Dp7-1, Dp306-1, Dp306-2, Dp306-3, DpH301, Dp1H23-1~Dp1H23-8 in the Dongping area, Nb1-1 in the Niuzhong area, N3 in the Niudong area, DT-1~DT-5 in the southern Datonggou area, and CSL-1~CSL-3 in the Caishiling area. These samples were firstly washed and trimmed and then pulverized and sieved with a 200 mesh. X-ray fluorescence spectrometry (Rigaku RIX 2100) was used for the analysis of major element compositions (relative standard deviation ranged from 2% to 8%). Next, the samples were digested using acid materials in Teflon bombs, and selected trace elements were analyzed by ICP-MS (Agilent 7500a with a shield torch) with analytical uncertainties of 1%–3%. The thermohistory of tectonic uplift was defined by a critical review of literature apatite/zircon fission track data [74].

4. Results

4.1. Quantification of the Weathering Crust

The characterization of the weathering crust was made by considering a variety of aspects including the depositional environment, geomorphology, crystalline structure, and the comparison of parent rocks [75,76]. Through the combination of petrological methods and a wireline log analysis, this study classified the structure of the weathering crust as: a soil layer, a complete weathering layer, a partial weathering layer–dissolution belt, a partial weathering layer–disintegration belt, and a nonweathering layer (parent rock layer) (Figure 3). With respect to the analysis of major elements, high concentrations of SiO_2, Al_2O_3, and Fe_2O_3 indicated the intensity of the weathering, whereas the concentrations of MgO and CaO in the weathering layer tended to be less than those in the soil layer and parent rock layer. CIA, CIW, and PIA have been commonly regarded as an indication of the extent of the weathering, but these criterions do not allow an identification of different layers [46–48]. As, Na, K, Ca, and Mg are mobile elements, thus the decrease in concentration of the related oxides is more likely to result from chemical leaching. During the incipient stage of the weathering, the oxides including Na_2O, K_2O, CaO, and MgO were largely lost from the profiles. On the contrary, elements including Al and Fe tend to concentrate in weathering products [39]. In this study, we propose the basement weathering index (BWI) to quantify the extent of the weathering (Table 2):

$$BWI = (Al_2O_3 + TFeO + TFe_2O_3)/(Na_2O + K_2O + CaO + MgO) \quad (1)$$

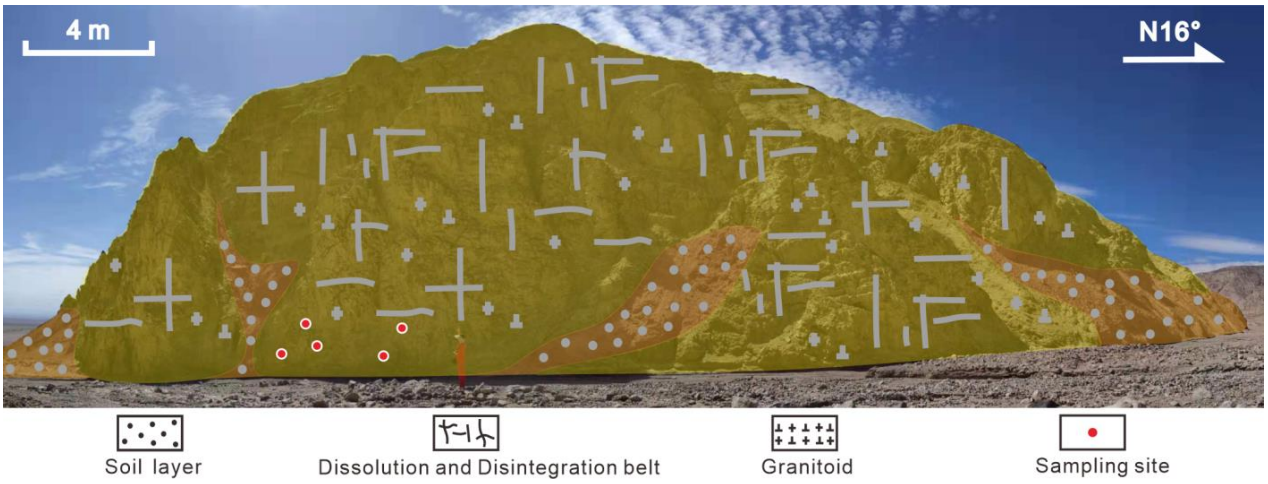

Figure 3. The weathering crust outcropped in the Datonggou area of the Qaidam Basin.

Table 2. Identification of weathering crust structure using weathering values.

Sample	CIA	CIW	PIA	BWI	Structure
Jb1-1	60.411	66.586	62.782	2.143	Partial Weathering
Jb1-2	53.800	59.476	54.696	1.814	Partial Weathering
Dp5-1	61.280	78.374	70.007	1.878	Partial Weathering
Dp7-1	66.076	83.789	77.852	2.173	Partial Weathering
Dp306-1	58.806	72.967	64.393	1.652	Partial Weathering
Dp306-2	60.761	74.903	67.290	1.789	Partial Weathering
Dp306-3	59.992	77.236	68.054	1.688	Partial Weathering
DpH301	60.430	77.041	68.337	1.760	Partial Weathering
N3	58.529	63.060	59.961	1.759	Partial Weathering
Nb1-1	61.271	76.967	69.035	1.843	Partial Weathering
Dp1H23-1	8.890	9.049	7.398	0.157	Nonweathering
Dp1H23-2	38.669	42.291	36.327	0.997	Nonweathering
Dp1H23-3	68.007	78.460	74.548	2.456	Complete Weathering
Dp1H23-4	46.865	52.019	46.091	1.017	Partial Weathering
Dp1H23-5	58.720	70.667	63.174	1.567	Partial Weathering
Dp1H23-6	63.198	82.911	75.164	1.910	Partial Weathering
Dp1H23-7	63.818	77.665	71.476	2.230	Partial Weathering
Dp1H23-8	64.351	79.075	72.867	2.237	Partial Weathering
DT-1	60.112	65.652	62.165	1.978	Partial Weathering
DT-2	58.972	77.289	67.056	1.635	Partial Weathering
DT-3	57.264	77.764	65.366	1.497	Partial Weathering
DT-4	59.368	64.662	61.202	2.097	Partial Weathering
DT-5	58.627	68.182	61.986	1.893	Partial Weathering
CSL-1	59.608	67.711	62.631	2.160	Partial Weathering
CSL-2	62.989	63.540	63.218	2.736	Complete Weathering
CSL-3	55.904	59.857	56.802	1.820	Partial Weathering

CIA: $100 \times Al_2O_3/(Al_2O_3 + Na_2O + K_2O + CaO)$; CIW: $100 \times Al_2O_3/(Al_2O_3 + Na_2O + CaO)$; PIA: $100 \times (Al_2O_3 - K_2O)/(Al_2O_3 + Na_2O + CaO - K_2O)$; BWI = $(Al_2O_3 + TFeO + TFe_2O_3)/(Na_2O + K_2O + CaO + MgO)$.

4.1.1. Soil Layer and Complete Weathering Layer

The soil layer (consisting of mudstone) was identified through the interpretation of imaging logs, including the stratification given by quartz bands and black bands with low resistivity (Figures 4a and 5a). The soil layer presented BWI values that were less than or equal to 1.0 (Table 2). The complete weathering layer, with a thickness of approximately 1.8 m to 32 m, was the transitional zone between basement rocks and sedimentary rocks deposited above. This layer was composed mainly of greywacke and granitic gneiss. Specifically, the greywacke consisted of alkali feldspar, quartz, and matrix, the rock structure of which showed line-to-line contacts and point-to-point contacts (Figure 4b). The granitic gneiss was crystallized with abundant alkali feldspar and biotite (Figure 4c,d) and a low content of quartz, whose undulating extinction could be due to mild tectonic deformation or compaction. The complete weathering layer contained more matrix, soil materials, and altered plagioclases when compared to other layers in the weathering crust. The authigenic minerals such as kaolinite, gypsum, and calcites were clearly seen in the granitic gneiss of the complete weathering layer. The values of the log data, including AC, GR, CNL, decreased from the top to the bottom of the wireline (Figure 5). Notably, where CNL decreased rapidly, RLLD and RLLS rose to a high level. High-resistivity bright spots and low-resistivity black spots were visible in the imaging logs as a response to the angular weather-resistant grains and residual clay minerals, respectively (Figure 5b). Due to deep weathering, the structure of the basement was completely lost; only some gypsum and carbonate bands were formed, which were identified as light bands through the imaging log. The complete weathering layer of granitoids showed a BWI value of more than 2.3 (Table 2).

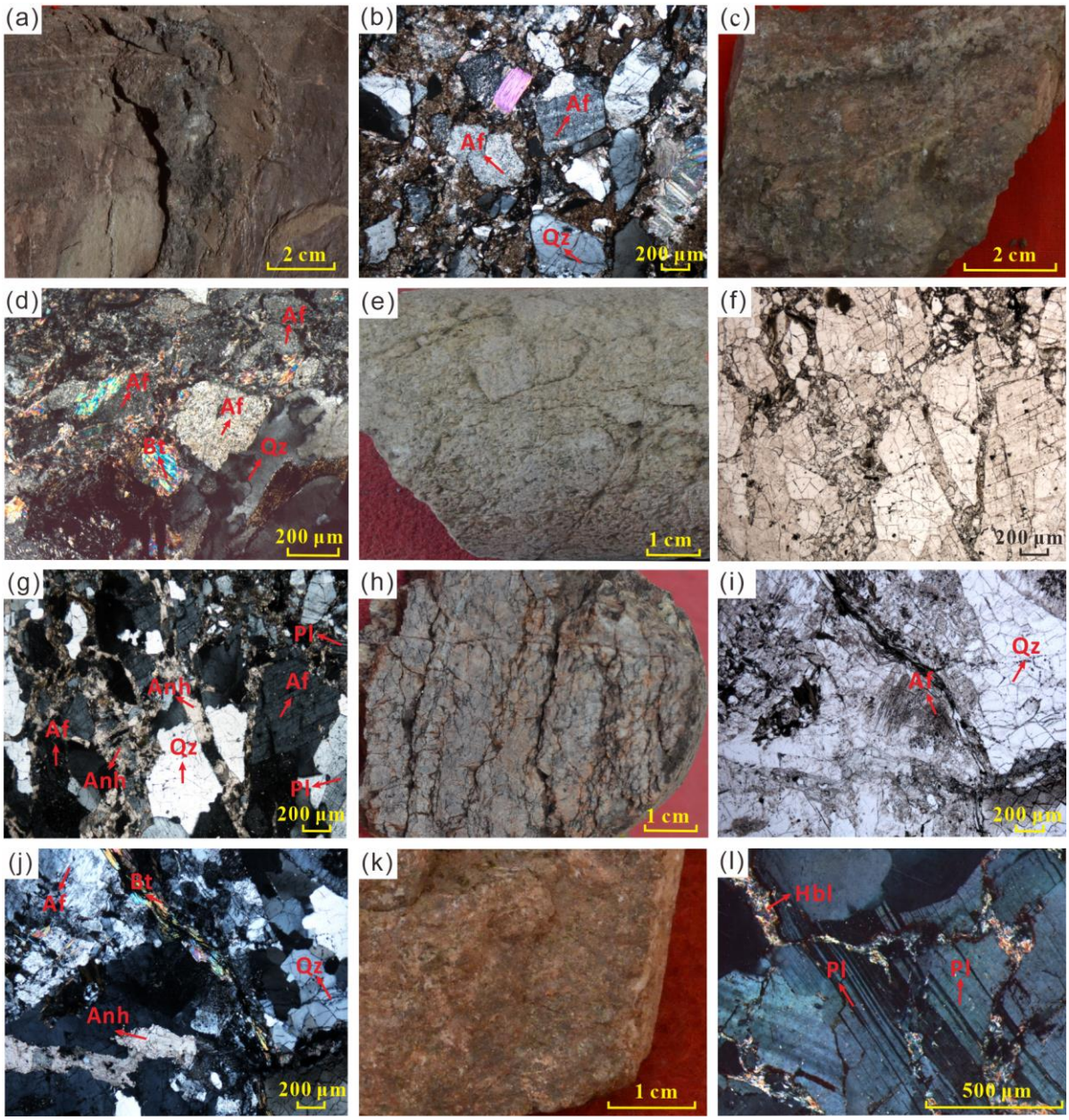

Figure 4. Petrography of granitoids that were exploited from distinct weathering crust belts. (**a**) Mudstone in soil layer, Dp1H23, 3070.88 m. (**b**) Greywacke in complete weathering layer, cross-polarized light, Dp1H23, 3075.48 m. (**c**) Granitic gneiss in complete weathering layer, Dp1H23, 3078.67 m. (**d**) Granitic gneiss in complete weathering layer, cross-polarized light, Dp1H23, 3078.67 m. (**e**) Granitoid in dissolution belt, N3, 2178.88 m. (**f**) Granitoid in dissolution belt, plane-polarized light, N3, 2178.88 m. (**g**) Granitoid in dissolution belt, cross-polarized light, N3, 2178.88 m. (**h**) Granite in disintegration belt, Dp306, 1907.8 m. (**i**) Monzonitic granite in disintegration belt, plane-polarized light, Dp306, 1916.76 m. (**j**) Monzonitic granite in disintegration belt, cross-polarized light, Dp306, 1916.76 m. (**k**) Granite in parent rock layer, Nb1, 3744.2 m. (**l**) Granite in parent rock layer, cross-polarized light, Nb1, 3744.2 m. Red arrows represent minerals. Qz: quartz, Af: alkali feldspar, Pl: plagioclase, Bt: biotite, Hbl: hornblende, Anh: anhydrite.

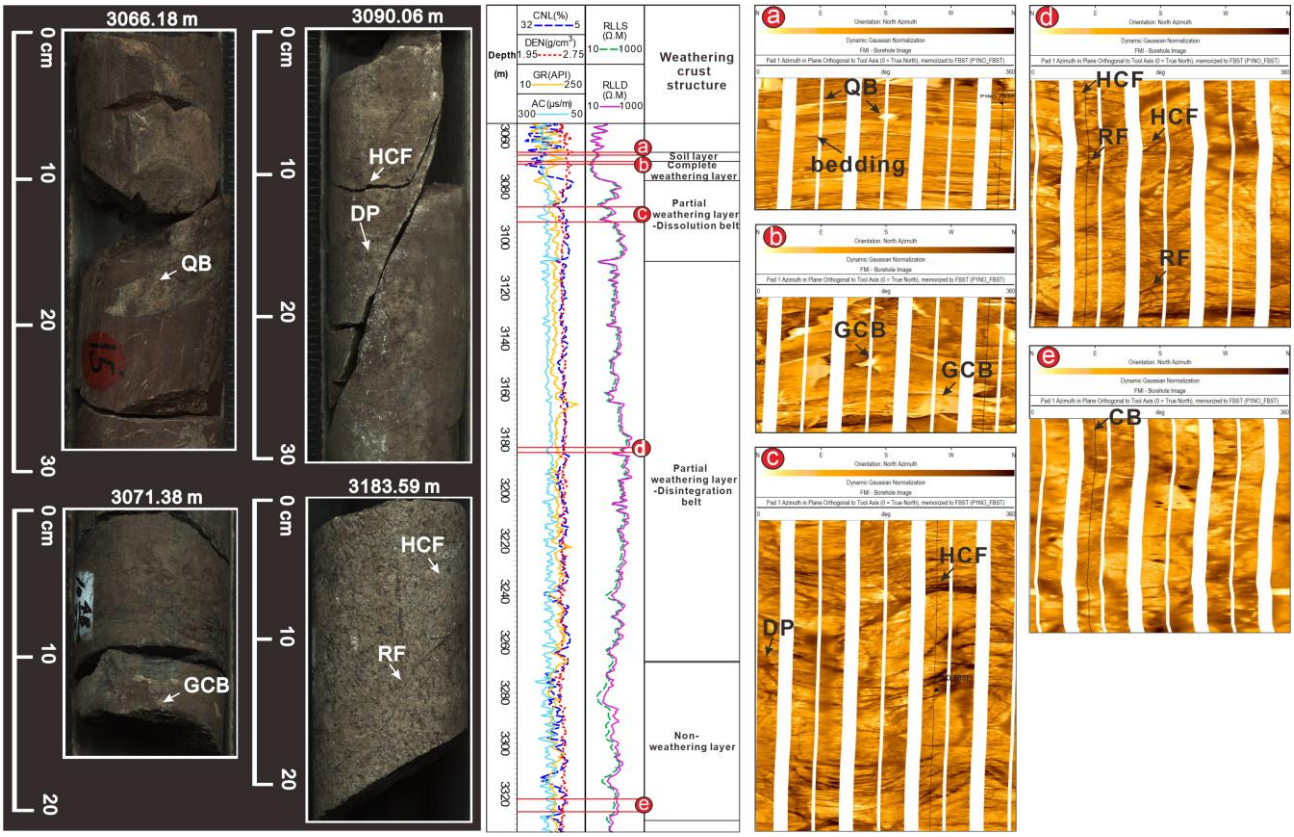

Figure 5. Characterization of weathering crust in granitoids through wireline logging data, taking well Dp1H23 as an example. (**a**) Soil layer in imaging log. (**b**) Complete weathering layer in imaging log. (**c**) Dissolution belt in imaging log. (**d**) Disintegration belt in imaging log. (**e**) Non-weathering layer in imaging log. QB: quartz band; GCB: gypsum and carbonate band; HCF: high-conductivity fracture; DP: dissolution pore; RF: reticular fracture; CB: cement band.

4.1.2. Partial Weathering Layer

Regarding the granitoids in the dissolution belt, most of the feldspars including alkali feldspar and plagioclase experienced dissolution, after which anhydrite was formed on feldspars or filled in the dissolution pores and fractures (Figure 4e–g). The thickness of the dissolution belt ranged from 30 m to 142 m. The log data such as GR and AC varied intensely when approaching the boundary between the compete weathering layer and the dissolution belt. Moreover, a sharp jump caused by a weak frequency and a small amplitude was visible in the wireline curves, with the sections with a box-shape plateau indicating deep dissolution. The dissolution belt still had the structure of the basement framework in the imaging logs, since it was only partially weathered. It could be observed that many high-conductivity sinusoidal fractures were connected to form a network. The edge of the fractures was blurred, partially due to dissolution broadening and large dark spots, indicating the low-resistivity areas where the dissolution pores or holes had developed (Figure 5c).

The disintegration belt was identified from the abundance of fractures, especially common in granitoids which are abundant in felsic materials (Figure 4h). As the felsic minerals included brittle, quartz, and feldspars, these were likely to be cracked by tectonic activity. The fractures formed during tectonic movements not only provide a way for leaching but also play an important role in the natural gas transportation. The alkali feldspars were replaced by kaolinites due to the alteration induced by acid meteoric water (Figure 4i). When meteoric water carrying sulfate materials passed through the fractures, some minerals such as anhydrite were crystallized in fractures or on the surface of feldspars (Figure 4j). Unlike other layers of the weathering crust, quartz cements were crushed to

broken grains during the interaction of later deep compaction and tectonic activities. The thickness of the disintegration belt was from 34 m to 194 m, with low baseline values in AC and a sharp curve showing a low frequency and small amplitude. The baseline values of GR, RLLD, and RLLS were high, while the lower parts of the above values indicated the sites where the fractures had developed. In the imaging logs, the fractures had a high conductivity, shown as dark stripes (Figure 5d). The dissolution belt and the disintegration belt had values of the BWI ranging from 1.0 to 2.3, which thus indicated the existence of the partial weathering layer (Table 2).

4.1.3. Nonweathering Layer

The granitoids in the nonweathering layer were abundant in plagioclase, with concavo-convex contact relationships. Some hornblendes formed on the edge of the feldspar grains, where no pores or effective fractures could be identified (Figure 4k,l). The RLLD and RLLS values of the nonweathering layer were lower than the values of the above disintegration belt. The CNL and AC values of the nonweathering layer increased slightly while the density (DEN), RLLS, and RLLD values decreased moderately compared with those in the disintegration layer. This layer also included no massive structure that resulted from weathering; however, some cement bands were generated within it (Figure 5e).

4.2. Reservoir Property Characterization

The reservoir spaces included matrix pores, dissolution pores, residual pores, and dissolution fractures that were developed mainly in the dissolution belt. The greatest contribution to the total porosity was given by the matrix porosity (approximately 70%) [77], which can have two different origins. Many dissolved matrix pores were developed within the clay minerals such as illite/smectite; these ranged in size between 124.4 nm and 689.0 nm (Figure 6a). Due to the crystallization which occurred in the mica, another type of matrix pore included intergranular pores and intragranular pores (Figure 6b). In comparison to the matrix pores, the dissolution pores were formed mainly in feldspar and the size of these pores tended to be much larger, ranging typically from 4 μm to 9 μm (Figure 6c). As a result of the interaction with acid meteoric water, the feldspars were usually replaced by kaolinites and thus, some residual pores were formed (Figure 6d). The residual pores, resulting from mineral alteration, were preserved among the aluminosilicate grains. Even though the fractures were not the dominant reservoirs in the dissolution belt, dissolution fractures could be observed in this layer, especially within the aluminosilicate minerals. The average width of the fractures that developed in the dissolution belt was from 6 μm to 2 mm, and those that were not filled with grains could be regarded as effective reservoirs (Figure 6e). With respect to the disintegration belt, more fractures resulting from tectonic activity developed in this belt than other layers, but some of them were filled with calcites or anhydrites (Figure 6f).

4.3. Physical Characteristics of Reservoirs

The results of the analysis of the physical properties from 123 cores showed that the granitoids developed low-porosity and low-permeability reservoirs. The porosity of the granitoids ranged from 0.50% to 9.76%, with an average value of 3.59%. The permeability of the granitoids in the study area ranged from 0.02 mD to 115.82 mD, with an average value of 1.98 mD (Figure 7). A clear correlation was identified between the porosity and the permeability of the granitoids.

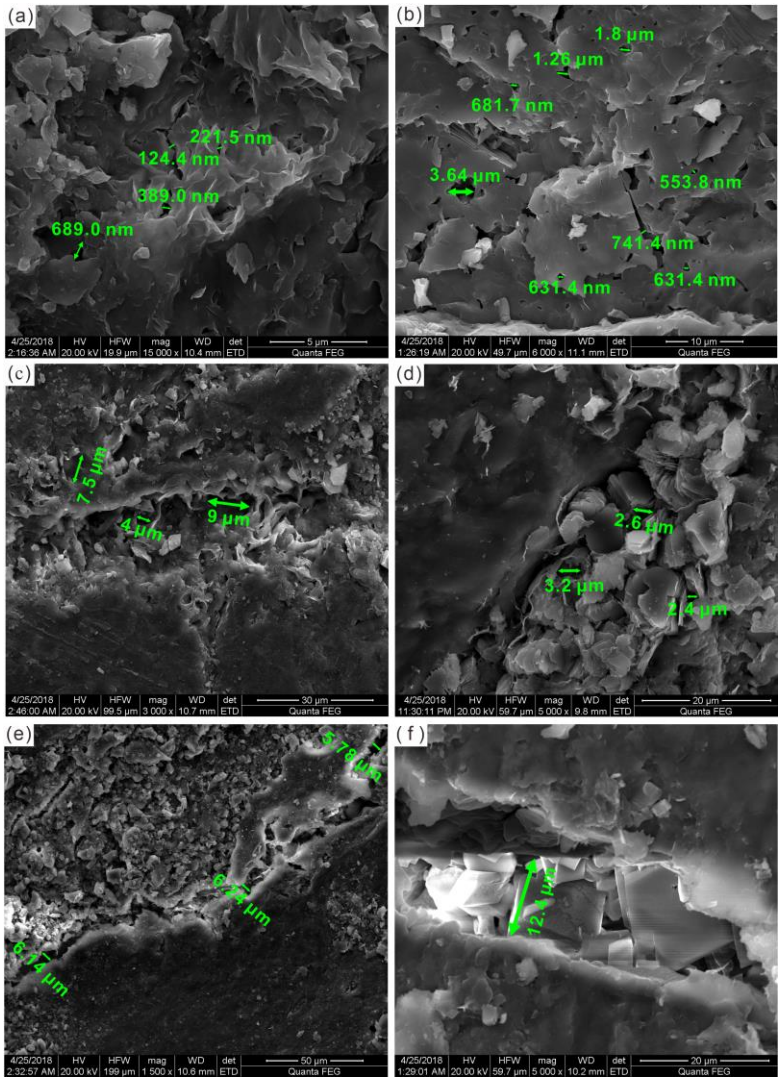

Figure 6. Reservoir characteristics of distinct weathering crust belts. (**a**) Dissolved matrix pores, Dp7, 2170.6 m; (**b**) Intergranular and intragranular matrix pores, Jb1, 4645.9 m; (**c**) Dissolution pores, N4, 998.2 m; (**d**) Residual pores, Nb1, 3742.37 m; (**e**) Dissolution fractures, N4, 998.2 m; (**f**) Tectonic fractures, South Datonggou, DT-1.

The reservoirs herein were classified as three types. The first type consisted of fractured-porous reservoirs that had a moderate porosity and permeability as shown in Figure 7. For this type of reservoir, the porosity usually varied from 1.56% to 8.48%, with a permeability which was significantly less than that of a fractured reservoir. The second type consisted of fractured reservoirs which had a porosity of no more than 5% and a permeability that was much higher than the other two types of reservoirs with the same porosity (Figure 7). The third type consisted of porous reservoirs that demonstrated a porosity ranging from 0.83% to 9.76%, while the permeability was so low that almost no fractures could possibly be found within rocks. Given these relationships between porosity and permeability, it is concluded that the granite mainly formed fractured-porous and fractured reservoirs, whereas the granitic diorite developed fractured-porous and porous reservoirs. Furthermore, the granitic gneiss held three types of reservoirs, but the most significant reservoir formed within the granitic gneiss was the fractured-porous reservoir (Figure 7).

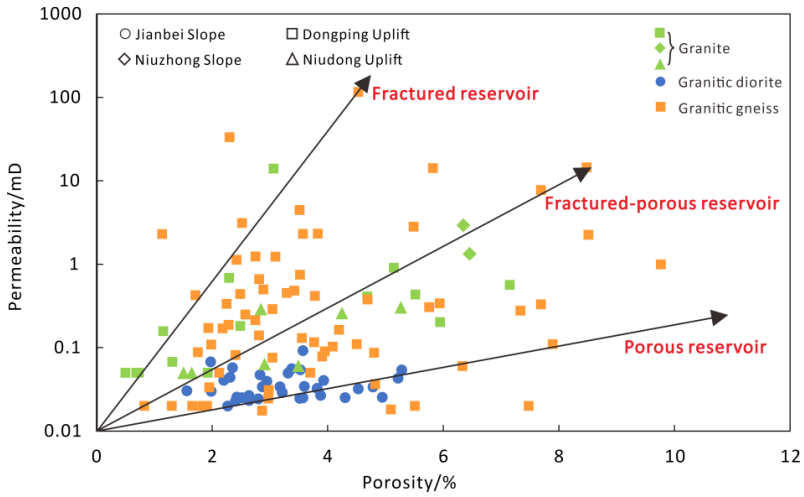

Figure 7. Cross-plot of the relationship between porosity and permeability of core samples from Qinghai oilfield.

5. Discussion

5.1. Contributions of the Weathering Crust to Reservoir Quality

5.1.1. Differentiation of Reservoir Quality

The presence of mechanical and chemical weathering extremely enhances the reservoir quality in granitoids. Hence, the weathering crust is the most feasible situation for the development of reservoirs [6]; this layer shows an increasing porosity and permeability with a decreasing distance from the top of the weathering crust [78]. In this study, however, the top of the weathering crust exhibited a low porosity and permeability due to materials formed under severe weathering conditions. Thus, high-quality reservoirs were more likely to be found in the partial weathering crust (Figure 8).

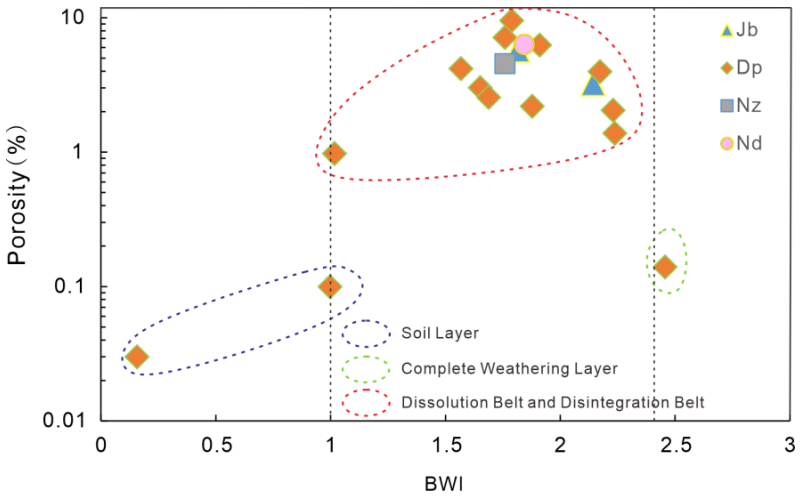

Figure 8. Cross-plot between BWI and porosity of the granitoids in north Qaidam. Jb: Jianbei Slope, Dp: Dongping Uplift, Nz: Niuzhong Slope, Nd: Niudong Uplift.

The soil layer and the complete weathering layer showed low porosity properties (Figure 8). The sediments of the soil layer were not affected by weathering, and diagenesis seldom occurred in this layer, such that it provided insufficient conditions for the formation of reservoirs. The complete weathering layer, with a low reservoir potential, was composed by up to 50% of matrix, soil materials, and some of the residual grains that formed after the weathering. The residual grains consisted of strongly altered plagioclases, with clear cleavage fractures and some matrix pores. Due to the deep weathering and leaching,

however, most of the unstable elements, including calcium, sodium, potassium, and magnesium, were mobilized from the parent rocks [47,48]. Reprecipitation occurred, facilitating authigenic minerals, including clay minerals, gypsum, and carbonate cements, to intermix and infill the cleavage fractures and matrix pores (Figure 9a).

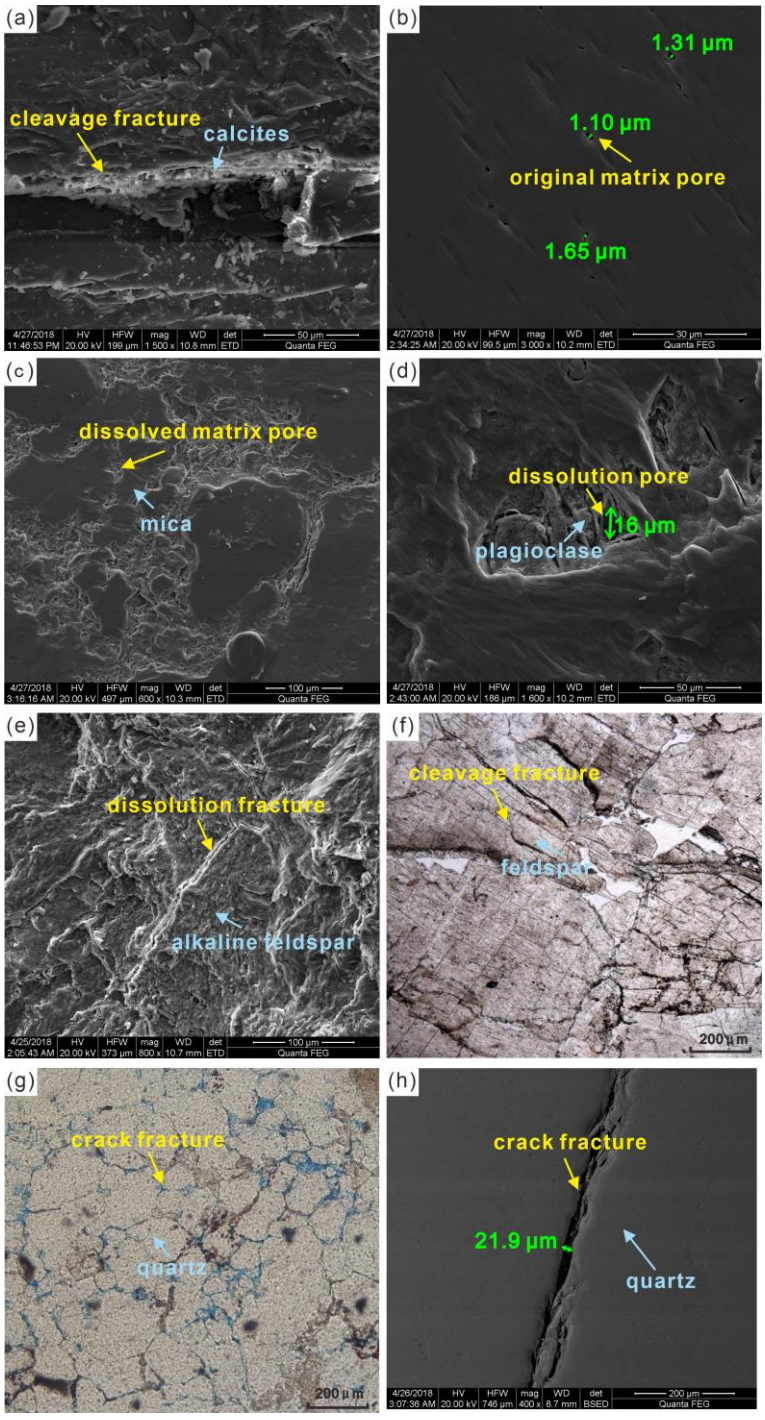

Figure 9. Reservoir characterization regarding different layers of weathering crust. (**a**) Cleavage fracture that is filled with calcites, Nb1, 3640.35 m; (**b**) Original matrix pores formed in quartz, Nb1, 3643.25 m; (**c**) Dissolved matrix pores formed with the mica carbonization, Dp103, 3230 m; (**d**) Dissolution pores in plagioclase, N4, 998.2 m; (**e**) Dissolution fractures formed in alkaline feldspars, DP7, 2170.6 m; (**f**) Cleavage fractures formed in the inner region of feldspars, Nb1, 3742 m; (**g**) Crack fractures that connect the intergranular pores in the margin of quartz, Jb1, 4647.95 m. (**h**) Crack fracture that cuts through the quartz, Dp123, 3360 m.

The porosity values of the cores analyzed from the dissolution belt or the disintegration belt ranged from 1.39% to 9.53%. The partial weathering layer was therefore the most feasible setting for the development of a granitoids reservoir. The matrix pores, dissolution pores, residual pores, and dissolution fractures provided the primary storage space for hydrocarbon accumulation in the Paleozoic granitoids. Specifically, the decomposition of feldspar, under the effect of chemical weathering, leads to a loss of Na_2O, CaO, and SiO_2 [79]. The decrease of oxides such as Na_2O and K_2O indicated that the rock had experienced an intense chemical weathering. The effects of weathering on granitoids can be characterized by the decomposition and the disintegration of the mineral phenocrysts and the formation of additional pores, especially in the vicinity of preserved fractures. The total porosity of these pores, including matrix pores, dissolution pores, and residual pores, was approximately 23.72%, which accounted for 31.6% of the entire reservoir porosity. In the case where the dissolution belt approached the top of the weathering crust, the weathering and leaching that occurred in that belt was stronger than what occurred in the disintegration belt, resulting in the formation of many dissolution fractures. The porosity measured in these dissolution fractures ranged from 0.29% to 7.33%, which contributed 28.10% to the total porosity. Consequently, the dissolution belt contained reservoirs which were of better quality than those developed in the disintegration belt. The statistical analysis of the porosity showed that the pores and dissolution fractures of the dissolution belt accounted for more than 50% of the total porosity.

5.1.2. Reservoir Generation Processes

The genesis of the reservoirs developed in the dissolution belt can be summarized as follows (Figure 10): (1) Two kinds of matrix pores were identified, including the original pores that were preserved after the crystallization, and the dissolved ones that could be ascribed to a later chemical alteration. The original matrix pores existed mainly in the quartz and mica (Figures 6b and 9b), while the dissolved matrix pores had several paths for their formation. Specifically, this type of matrix pore was developed not only in felsic granitoids but also in granitic gneisses. The felsic granitoids were crystallized with large amounts of aluminosilicate minerals. Clay minerals such as illite, smectite, and kaolinite were formed after the alteration of alkaline feldspars, facilitating the development of pores of nanoscale magnitude (Figure 6a). Regarding the granitic gneiss, one type of dissolved matrix pore resulted from the alteration of biotite or hornblende, above which the chlorites were identified, and the matrix pores were situated along the edge of Fe/Mg-bearing minerals. Furthermore, some matrix pores were formed under the influence of alkaline underground flows, especially in the case of mica. As a result of the interaction with alkaline flows, the carbonization which induced the matrix pores could be identified (Figure 9c). The calcite cements were formed with the recrystallization, under the influence of acid fluids; the dissolution occurred within calcites with some matrix pores developing especially in the middle diagenesis stage [80]. (2) The dissolution pores were formed under the action of fluid flows that moved through the tectonic fractures or were preserved under the ground surface. Due to chemical interaction with the plagioclase, the sericites or chlorites were developed as well as some dissolution pores which were located within these minerals (Figure 9d). Furthermore, the residual pores were preserved along the edge of the authentic minerals after the feldspar alteration (Figure 6d). Another type of dissolution pore was formed mainly after the alteration process that occurred inside the alkaline feldspars. The clay minerals including kaolinite, illite, and smectite were developed subsequently and the dissolution occurred in the presence of underground flows (Figure 6c). (3) Under the influence of alkaline groundwater or flows containing sulfites, the felsic minerals, especially the aluminosilicate ones, were likely to have been dissolved (Figure 6e). The dissolution fractures here could be widely observed and some of them were filled with calcites or anhydrites (Figure 9e). The effective fractures were those not infilled with minerals that connected with each other or with the other pores.

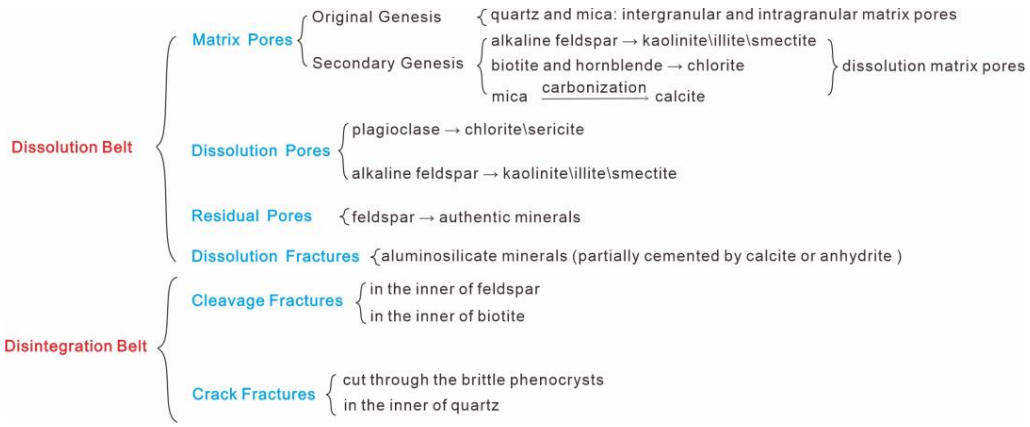

Figure 10. Genesis of reservoirs in distinct weathering crust layers.

It can be speculated that, due to mechanical weathering, the cleavage fractures were widened and distributed commonly within the feldspars (Figure 9f). The cleavage fractures are more likely to be found in the feldspars of the granitoids, while the granitic gneiss is a favorable situation for the formation of cleavage fractures in the biotite. Although some of the cleavage fractures were filled with calcites or gypsum, they contributed approximately 15% to the total porosity. Another type was made up of crack fractures that bypassed the edge of the mineral grains or cut through the phenocrysts. The original pores were distributed irregularly within the rocks and seldom formed effective throats to connect with each other, but the crack fractures that are commonly developed in the margin of minerals served as an effective channel to connect the intergranular pores among quartz grains (Figure 9g). Meanwhile, other crack fractures that cut through the grains without any filling of authigenic minerals showed a good connectivity, which meant these fractures had a positive effect on the hydrocarbon accumulation (Figure 9h). Brittle minerals are readily cracked under tectonic stress [81]. This type of crack fracture can be extensively observed in quartz, which exists not only in granite and granitic diorite but also in granitic gneiss. Due to the plastic deformation of mica, crack fractures are less likely to be formed inside phyllosilicate minerals. Thus, it can be concluded that the granitoids which contain more felsic grains are the more favorable place for the development of structural fractures. Overall, the crack fractures contributed 25.3% to the total reservoir porosity.

5.2. Controlling Factors of Weathering Crust Reservoirs

5.2.1. Lithology and Mineral Composition

The complete weathering layer is regarded as a cap for reservoirs that inhibits the natural gas from escaping. The lacustrine mudstone and the basement rocks, which are filled with gypsum and calcite, act as cap rocks [23], while the parent rocks play a crucial role in the process of weathering, especially for their mineral components and soluble constituents [25]. This research showed that the dissolution of granite was not as extensive as in the case of granitic gneiss and granitic diorite. The thickness of the weathering crust in femic granitoids was much greater than that found in the felsic granitoids (Table 3). According to the reservoir properties of granite and granitic gneiss (Figure 11), the porosity of granite was usually less than 2%–3% (these granites contributed 52.17% to the total amount of granites), while the porosity of granitic gneiss was mostly more than 2%–3% (the amount that granitic gneiss contributed to the total amount of granitic gneiss was 56.01%). Due to the presence of brittle minerals, the granites should be more likely to crack within and to form crack fractures, but the permeability distribution between granite and granitic gneiss was almost the same. Up to 73.91% of granites had a permeability that was less than 0.50 mD and 72.72% of granitic gneiss had a similar value. We deduced that even though the granite was more prone to develop fractures due to its felsic components, the gneissose structure in granitic gneiss could also facilitate the format ion of fractures,

likewise resulting in enhanced permeability. Even though the felsic and femic granitoids had a similar permeability, the femic granitoids had a thicker disintegration belt, which implied that some authentic minerals had infilled some of the fractures and thus reduced the level of permeability.

Table 3. Thickness variation of distinct weathering crust structures regarding different lithological components.

Thickness/m / Weathering Crust Structure	Felsic Granitoids			Femic Granitoids		
	Min	Max	Avg	Min	Max	Avg
Complete weathering layer	3.32	32.76	13.89	1.81	21.23	11.97
Dissolution belt	30.12	100.04	58.22	35.22	142.54	86.57
Disintegration belt	34.00	114.16	65.84	48.02	194.65	103.43

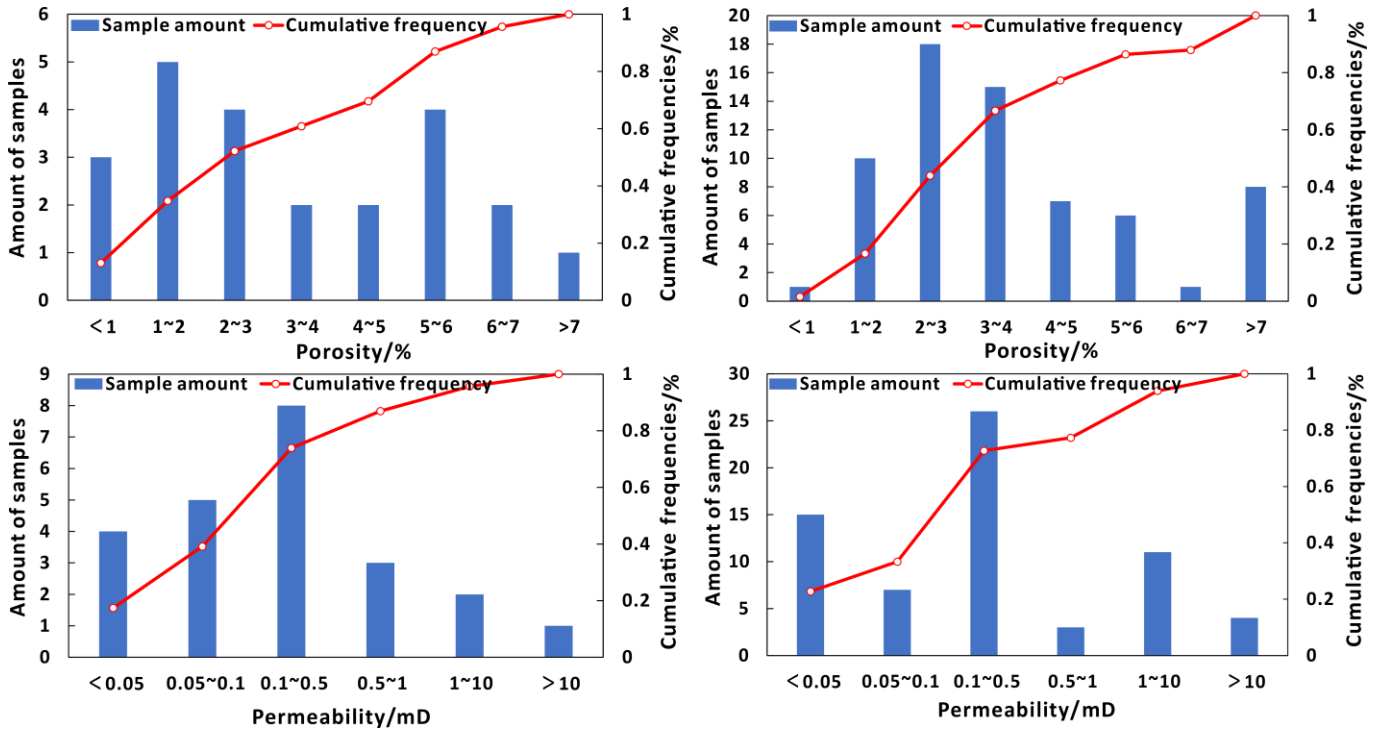

Figure 11. Physical properties of granite and granitic gneiss. (**a**) The distribution of porosity of granite; (**b**) the distribution of porosity of granitic gneiss; (**c**) the distribution of permeability of granite; (**d**) the distribution of permeability of granitic gneiss.

5.2.2. Tectonic Uplift

The Qaidam Basin was affected by multiple uplift episodes from the Triassic to the Miocene as deduced by thermochronology datasets and regional tectonic background [59,82–85]. The detached fault near the Altyn Tagh Range was active from the late Triassic to the early Jurassic, corresponding to the cooling event during this period in northern Tibet [86,87]. According to the fission-track analysis of zircon and apatite (ZFT and AFT) within crystalline-basement rocks, the north Qaidam Basin experienced a tectonic uplift from the late Triassic to the early Jurassic, followed by a rapid erosion during the Jurassic [83]. Other AFT and ZFT data indicate that the northwestern Qaidam Basin was uplifted from 133.7 ± 6.6 Ma to 39.1 ± 9.3 Ma [88].

During the early Middle Jurassic, the Qaidam Basin was in an extensional tectonic regime after a collision occurred among several blocks in Northwest China [89]. The onset of the Paleo-Tethys Ocean could be the main factor for the formation of the rift basins in the early Jurassic, which also led to the presence of an extensional stress field in western

Qaidam Basin until the Middle Jurassic [65]. The Yanshanian orogenic event was sustained from the late Jurassic to the Cretaceous. It caused the convergence between the Gangdise Plate and the Qiangtang Plate, the collision between the Huabei Plate and the Siberia Plate, and the closure of Tethys Ocean [90,91]. In this period, the Qaidam Basin underwent extrusion, depression, and uplift. The north block located in front of the Altyn Mountain was uplifted while the south block was lowered, which led to the strata of the north block experiencing intense weathering during the late Mesozoic period. The Jurassic exhumation was followed by a phase of sedimentation in the Cretaceous [83], except for the region along the Altyn Tagh Fault. From the Cretaceous to the Cenozoic, several episodes of cooling were recorded by low-temperature thermochronology [88,92–94]. The early Cretaceous denudation was followed by a tectono-thermal event occurring from the Oligocene to the Miocene. This latter event might correspond to strike-slip tectonics along the Altyn Fault and furthermore, it could also be responsible for the initial formation of the high relief of north Tibet [53,83]. In the north Qaidam Basin, a regional unconformity marks the end of the Jurassic (Figure 2). This unconformity represents the top boundary of the weathering crust, above which the sedimentary materials (Lulehe Formation) such as mudstones and gypsolyte were deposited in the Paleogene. The missing strata (from the late Jurassic to the Cretaceous) correspond to an exhumation phase in the Altyn Fault terrane (Figure 12a,c), which facilitated the development of the weathering crust of the basement rocks in the north Qaidam Basin.

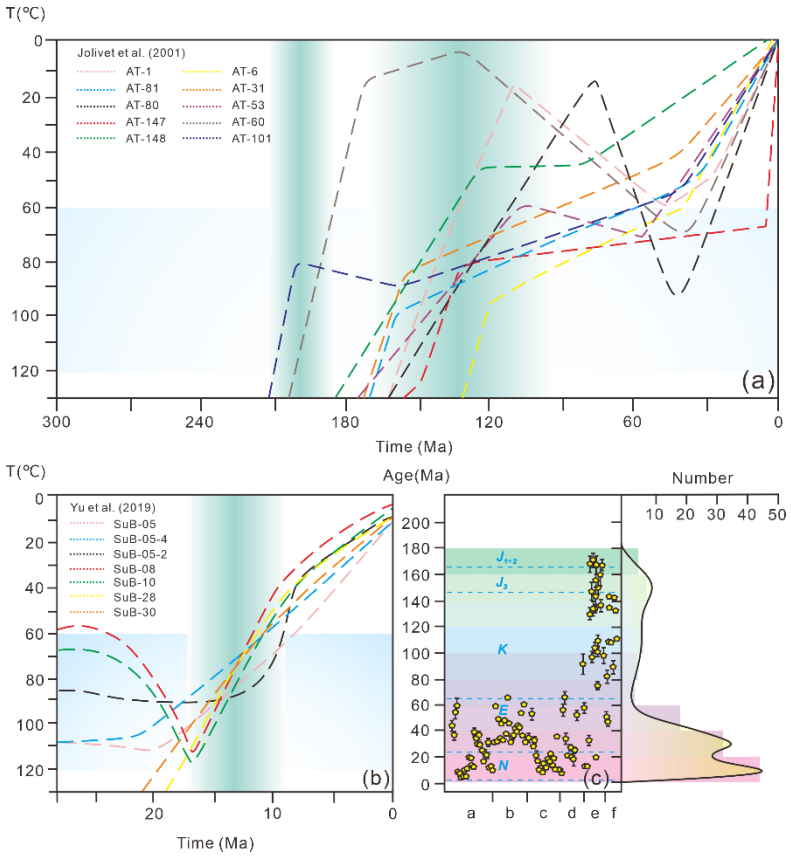

Figure 12. Thermal modeling results and thermochronology dataset from the block along Altyn Fault belt: (**a**,**b**) compiled from Jolivet et al. [83] and Yu et al. [95], dotted lines indicate the expected model results. (**c**) Fission track analysis of apatites and zircons in the area of Altyn Fault belt; thermochronology data are from a. Chen et al. [96], b. Sun et al. [97], c. Wan et al. [98], d. Wang et al. [99] and Wang et al. [100], e. Jolivet et al. [83], f. Peng [101]. Apatites and zircons used in fission track analysis were fully or partially thermally reset.

5.2.3. Faulting

During the Himalayan orogenesis, especially from the Neogene to the Quaternary, the strike-slip faults that affect the north Qaidam region were formed [102,103]. Zou et al. [26] proposed that the density of fractures depended on their distance from primary faulting zones and that these faults had controlled the distribution and the strike of fractures developed within the weathering crust. In this study, we selected sampling wells near the faulting zone to understand the relationships between fractures and the reservoir properties in granitoids (Figure 13). The thickness of the disintegration belt was larger than that of the dissolution belt in samples from wells such as Nb2 and Nb3; moreover, these samples were from the same paleogeography (Figure 14). Based on the regional tectonic background and thermal modeling results, the Altyn region underwent accelerated exhumation from the late Oligocene to the early Miocene (Figure 12b,c) and, eventually, represented the onset of a transition along the Altyn Tagh Fault from a left-lateral strike-slip motion to a crustal shortening [95]. The reservoirs developed in the disintegration belt were probably induced by tectonic deformation in the early Middle Cenozoic.

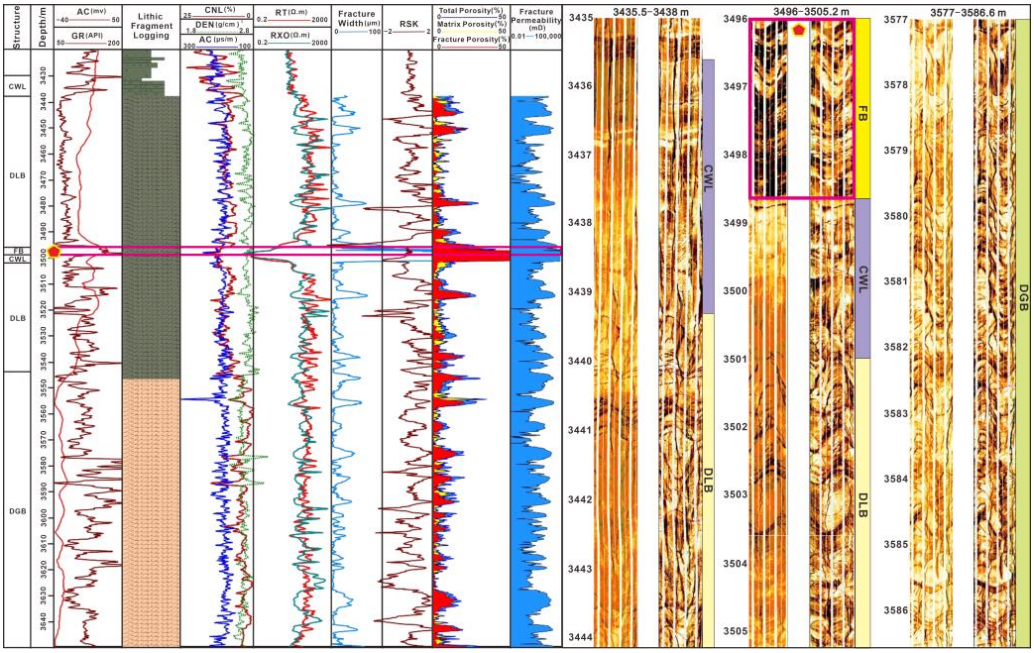

Figure 13. Identification of fault belts and characterization of their physical properties from the logging dataset. CWL: complete weathering layer, FB: fault belt, DLB: dissolution belt, DGB: disintegration belt.

5.2.4. Paleogeomorphology

The total thickness of the partial weathering layer in distinct paleogeomorphology settings was identified in this study because of its crucial role in the capacity of weathering crust reservoirs. Samples that had similar lithology were selected to highlight the paleogeomorphological controls on the development of the weathering crust reservoirs. Apart from the wells situated close to the faults, the thickness of partial weathering crust developed on the slopes (well Dp306, Dp5, Dp7, Nb1) was larger than that developed in the depressions (well Dp4, Jb4). Regarding the slope, the granitoids developed in higher areas showed a higher quality of reservoir than in the lower areas of the slopes (Figure 14). With respect to the wells in similar paleogeomorphological areas, there were no evident relationships between the dissolution belt and the distinction belt for the felsic granitoids and femic granitoids, possibly due to the influence of adjacent major faults. The topographical highs were in a strong denudation zone where the weathering denudation rate was greater than the formation rate of the weathering crust, and thus the complete and partial weathering

zone were not well presented [26]. As the weathering and denudation of the slopes were weaker than on topographical highs, the complete weathering layer in the slope sections was retained and, therefore, the partial weathering zone had the possibility to develop. Meanwhile, in the depressions, large volumes of weathering residuals were accumulated and formed a complete weathering layer of a large thickness. This complete weathering layer hindered the surface water penetrating downward to erode the strata below, thus the leaching effect was weak, and the thickness of the weathering crust in the depression area was relatively thin.

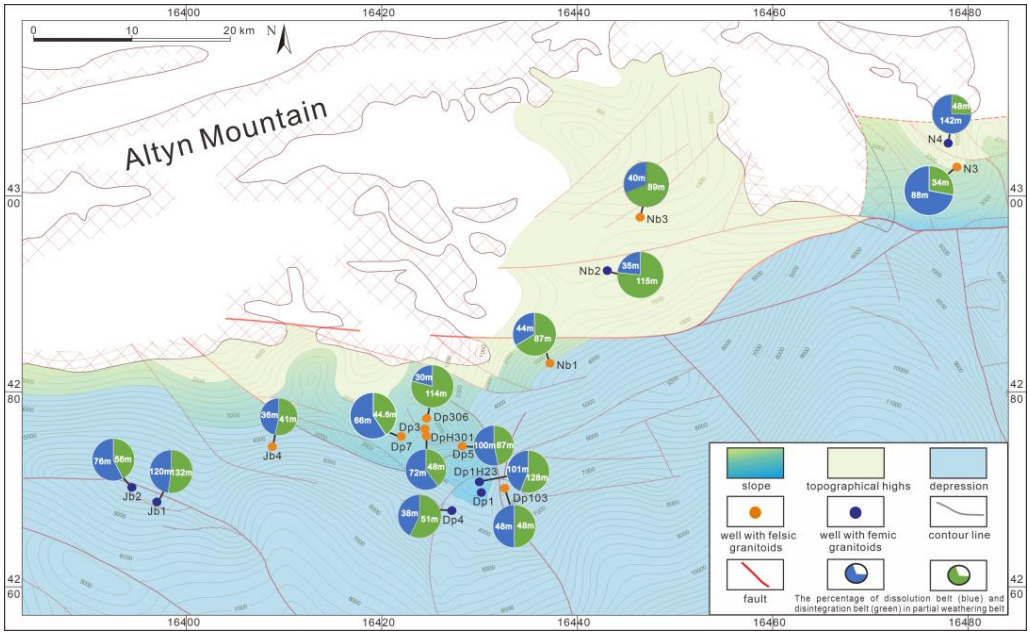

Figure 14. Thickness variation of partial weathering crust layer and its relationships among lithology, tectonism, and paleogeomorphology (the contour values of paleogeomorphology are interpreted based on the T6 reflection layer of seismic data; these values represent the height of the basement top before the deposition above).

5.3. Reservoir Modeling and Natural Gas Implications

Based on factors such as reservoir-space systems, physical properties, lithology, faulting, and paleogeomorphology, the appraisal of granitoid reservoirs in front of the Altyn Mountain was classified into three types as outlined below (Table 4), including Type I (highest reservoir quality), Type II (moderate reservoir quality), and Type III (poor reservoir quality). The reservoir system herein described contained proven resources as demonstrated by the hydrocarbon test results from the dissolution belt (Figure 15): the daily production of natural gas from Dp3 at depths of 1850 m to 1870 m was 0.7181 $\times$ 10^4 m^3, while Dp1 had a natural gas production of 15.97 $\times$ 10^4 m^3 per day from depths of 3159 m to 3182 m. Both granitoids in Dp3 and Dp1 were situated in the slope zone, but the granitoid in Dp3 was granite whereas Dp1 was drilled in granitic gneiss. The porosity of the granitoids in Dp3 and Dp1 were 2.59% and 6.00%, respectively, and the permeability of the granitoids were 5.20 mD and 0.01 mD, respectively. The parameters analyzed above can be classed as corresponding to basement reservoirs of the highest quality (I).

Table 4. Appraisal parameters of the granitoid reservoirs in Qaidam Basin.

Reservoir Quality	I	II	III
Reservoir Type	Fractured-porous reservoir	Porous reservoir	Fractured reservoir
Porosity/%	1.562–8.479	0.825–9.763	0.498–4.528
Permeability/mD	0.0304–14.478	0.020–0.995	0.050–115.816
Lithology	Granitic gneiss (23.58%), granite (10.57%), granitic diorite (4.88%)	Granitic diorite (21.95%), granitic gneiss (17.89%), granite (3.25%)	Granitic gneiss (12.20%), granite (5.68%)
Palaeogeomorphology (contour value/m)	Slope (2000–3400)	topographical highs (1000–2000)	depression (>3400)
Representative wells	Dp106, DpH301, Dp123, Dp1H23, Dp306, Dp5, Dp1, Dp3, N3, Nb1, Jb1	Dp106, DpH301, Dp123, Dp1H23, DpH101, Jb1	Dp106, DpH301, Dp306, Dp5, Dp123, Dp1H23

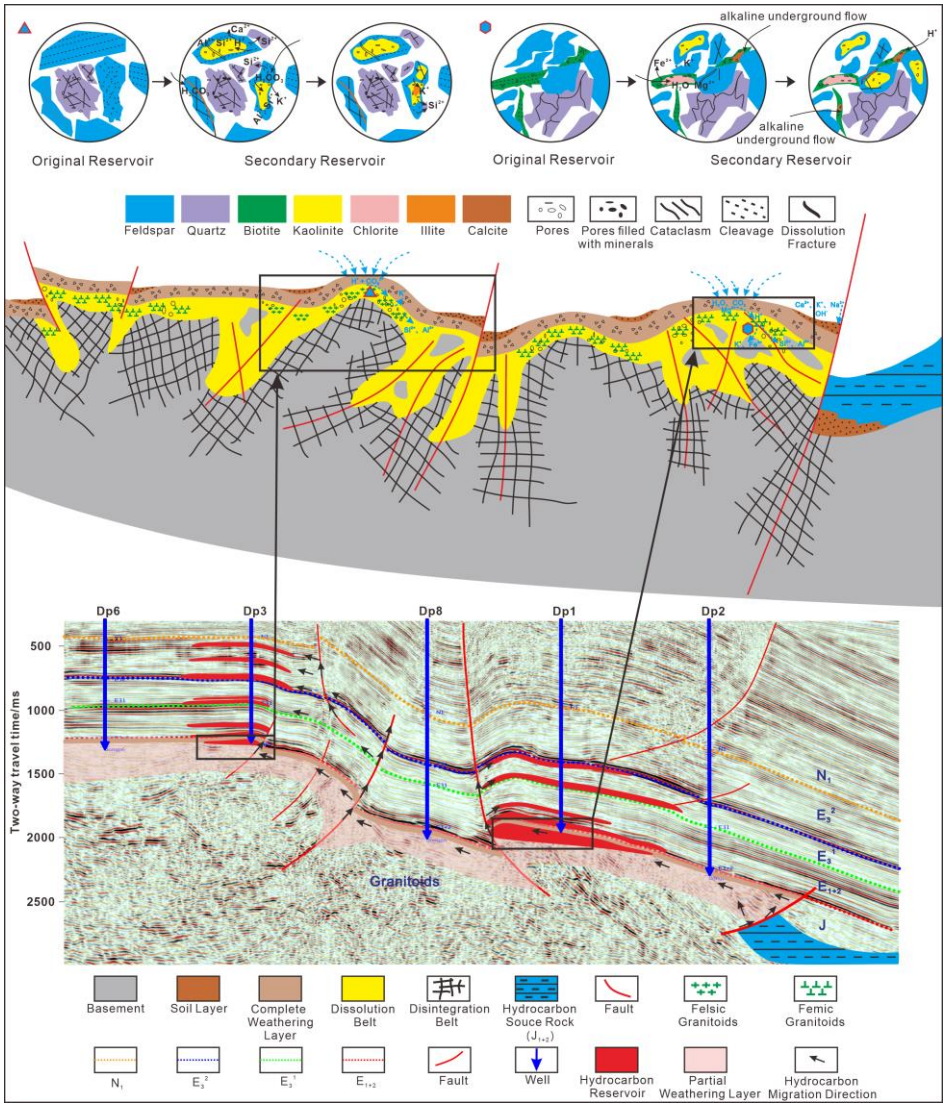

Figure 15. Mechanism model of the granitoids reservoir in Qaidam Basin (the data of the hydrocarbon reservoir were tested at the PetroChina Qinghai oilfield).

6. Conclusions

(1) The structure of the weathering crust was classified as complete weathering layer, partial weathering layer (dissolution belt and disintegration belt), and nonweathering layer based on the occurrence of different minerals, elements, and textures in the rocks, as well as the interpretation of logging datasets. The top to middle section of

the partial weathering crust, where the majority of the observed pores and fractures had developed, demonstrated the most advantageous reservoir physical properties.

(2) The dissolution belt was characterized by matrix pores, dissolution pores, residual pores, and dissolution fractures. The matrix pores represented the most important contribution to the total porosity. The clay minerals such as illite/smectite generated abundant dissolved matrix pores. Another type of matrix pore included intergranular pores and intragranular pores, which were formed mainly due to the crystallization of mica. The sericites or chlorites, together with some dissolution pores, developed because of the chemical interactions that occurred within the plagioclase. The residual pores were preserved among the aluminosilicate grains, whereas dissolution fractures were formed within them. More cleavage fractures and crack fractures were formed in the disintegration belt, but some of those were filled with calcites or anhydrites.

(3) The femic granitoids, including granitic gneiss and granitic diorite, were appropriate lithologies for the formation of reservoirs due to the possible intense dissolution in these rocks. The felsic granitoids had a greater fracture potential. The gneissose structure greatly enhanced the permeability of granitic gneiss. No clear relationships were observed between the quality of the reservoirs in the dissolution and the disintegration belts and the presence of femic and felsic granitoids. The thickness of the partial weathering layer in femic granitoids, however, was larger than that in felsic granitoids.

(4) Faulting was the main factor for the formation of the disintegration belt, which was induced mainly by the tectonic deformation occurring from the late Oligocene to the early Miocene in Altyn Fault belt. The reservoir quality seemed to be greater when the granitoids had developed close to the main fractures. Therefore, the dissolution belt was controlled by faulting, and to some extent, the mode in which the fractures connected the pores together. The paleogeomorphology influenced the extent of the weathering, from which the thickness of the weathering crust in the slope areas was larger compared to that in depression areas. The exhumation that took place from the late Jurassic to the Cenozoic in Altyn terrane corresponded to the weathering and leaching period of the granitoids.

(5) The reservoirs in granitoids could be classified into three types: fractured-porous, porous, and fractured. The fractured-porous type was associated with the best capacity of reservoirs found in granitoids, and this type developed mainly in the dissolution belt of the weathering crust. Therefore, the dissolution belt was the predominant zone of high-quality granitoid reservoirs, in which the total porosity of pores and dissolution fractures accounted for 59.7% of the entire reservoir porosity.

Author Contributions: Conceptualization, X.J. and H.N.; methodology, X.J., H.N. and Q.X.; software, Y.Z. and Z.W.; validation, X.J., H.N. and Q.X.; formal analysis, X.J.; investigation, X.J. and H.N.; resources, Y.Z.; data curation, X.J. and Z.W.; writing—original draft preparation, X.J.; writing—review and editing, X.J., H.N., M.Z., Z.W., Y.C., X.Z., S.L. and X.W.; visualization, X.J. and Z.W.; supervision, H.N.; project administration, Q.X. and Y.Z.; funding acquisition, Q.X. All authors have read and agreed to the published version of the manuscript.

Funding: The work in the manuscript is funded by National Major Science and Technology Project of China National Petroleum Corp. (grant No. 2017ZX05063002-006) and the Beijing Higher Education Young Elite Teacher Project (grant No.YETP0669). Xiaoqin Jiao is funded by the China Scholarship Council (202006440023).

Data Availability Statement: Data are contained within the article.

Acknowledgments: This work was co-funded by the National Major Science and Technology Project of China National Petroleum Corp. (grant no. 2017ZX05063002-006) and the Beijing Higher Education Young Elite Teacher Project (grant no. YETP0669). Xiaoqin Jiao was funded by the China Scholarship Council (202006440023). We thank the Exploration and Development Institute of Qinghai Oilfield Company, CNPC, China, for their collaboration and for providing some data in this study. We express our thanks to Tegan Blount for refining the English language of the manuscript.

Conflicts of Interest: The authors declare no conflict of interests.

References

1. Walters, R.F. Oil Production from Fractured Pre-Cambrian Basement Rocks in Central Kansas. *AAPG Bull.* **1953**, *37*, 300–313. [CrossRef]
2. P'an, C.H. Petroleum in Basement Rocks. *Am. Assoc. Pet. Geol. Bull.* **1982**, *66*, 1597–1643. [CrossRef]
3. Smith, J.E. Basement Reservoir of La Paz-Mara Oil Fields, Western Venezuela. *AAPG Bull.* **1955**, *40*, 380–385.
4. Landes, K.K.; Amoruso, J.J.; Charlesworth, L.J.; Heany, F.; Lesperancep, J. Petroleum Resources in Basement Rocks: Discussion. *AAPG Bull.* **1961**, *45*, 1682–1691. [CrossRef]
5. Areshev, E.G.; Dong, T.L.; San, N.T.; Shnip, O.A. Reservoirs in Fractured Basement on the Continental Shelf of Southern Vietnam. *J. Pet. Geol.* **1992**, *15*, 451–464. [CrossRef]
6. Ma, F.; Yang, W.; Zhang, Y.; Li, H.; Xie, M.; Sun, X.; Wang, P.; Bai, Y. Characterization of the Reservoir-Caprock of the Large Basement Reservoir in the Dongping Field, Qaidam Basin, China. *Energy Explor. Exploit.* **2018**, *36*, 1498–1518. [CrossRef]
7. Seemann, U.; Scherer, M. Volcaniclastics as Potential Hydrocarbon Reservoirs. *Clay Miner.* **1984**, *19*, 457–470. [CrossRef]
8. Schutter, S.R. Hydrocarbon Occurrence and Exploration in and around Igneous Rocks. *Geol. Soc. Spec. Publ.* **2003**, *214*, 7–33. [CrossRef]
9. Cuong, T.X.; Warren, J.K. Bach Ho Field, a Fractured Granitic Basement Reservoir, Cuu Long Basin, Offshore SE Vietnam: A "Buried-Hill" Play. *J. Pet. Geol.* **2009**, *32*, 129–156. [CrossRef]
10. Parnell, J.; Baba, M.; Bowden, S.; Muirhead, D. Subsurface Biodegradation of Crude Oil in a Fractured Basement Reservoir, Shropshire, UK. *J. Geol. Soc.* **2017**, *174*, 655–666. [CrossRef]
11. Adepelumi, A.A.; Yi, M.J.; Kim, J.H.; Ako, B.D.; Son, J.S. Integration of Surface Geophysical Methods for Fracture Detection in Crystalline Bedrocks of Southwestern Nigeria. *Hydrogeol. J.* **2006**, *14*, 1284–1306. [CrossRef]
12. Stober, I.; Bucher, K. Hydraulic Properties of the Crystalline Basement. *Hydrogeol. J.* **2007**, *15*, 213–224. [CrossRef]
13. Zou, C.N.; Hou, L.H.; Yang, F.; Yang, C.; Tao, S.Z.; Yuan, X.J.; Zhu, R.K. Structure of Weathered Clastic Crust and Its Petroleum Potential. *Sci. China Earth Sci.* **2014**, *57*, 3015–3026. [CrossRef]
14. Ma, L.; Liu, Q.X.; Zhang, J.L.; Wei, P.S.; Chen, Q.L.; Zhang, H.Q. A Discussion of Exploration Potentials of Basement Hrdrocarbon Reservoir. *Nat. Gas Ind.* **2006**, *26*, 8–11, (In Chinese with English abstract).
15. Sunarjanto, D.; Widjaja, S. Potential Development of Hydrocarbon in Basement Reservoirs In Indonesia Pengembangan Potensi Reservoir Hidrokarbon Batuan Dasar Di Indonesia. *Indones. J. Geosci.* **2013**, *8*, 151–161.
16. Frey, M.; Ebbing, J. The Deep Geothermal Potential of the Radiogenic Løvstakken Granite in Western Norway. *Nor. J. Geol.* **2020**, *100*, 1–27. [CrossRef]
17. Achtziger-Zupančič, P.; Loew, S.; Hiller, A. Factors Controlling the Permeability Distribution in Fault Vein Zones Surrounding Granitic Intrusions (Ore Mountains/Germany). *J. Geophys. Res. Solid Earth* **2017**, *122*, 1876–1899. [CrossRef]
18. Zeng, Y.; Tang, L.; Wu, N.; Cao, Y. Numerical Simulation of Electricity Generation Potential from Fractured Granite Reservoir Using the MINC Method at the Yangbajing Geothermal Field. *Geothermics* **2018**, *75*, 122–136. [CrossRef]
19. Doetsch, J.; Krietsch, H.; Schmelzbach, C.; Jalali, M.; Gischig, V.S.; Villiger, L.; Amann, F.; Maurer, H. Characterizing a decametre-scale granitic reservoir using ground-penetrating radar and seismic methods. *Solid Earth.* **2020**, *11*, 1441–1455. [CrossRef]
20. Ye, T.; Chen, A.; Niu, C.; Wang, Q.; Guo, L. Characteristics and Vertical Zonation of Large-Scale Granitic Reservoirs, a Case Study from Penglai Oil Field in the Bohai Bay Basin, North China. *Geol. J.* **2020**, *55*, 8109–8121. [CrossRef]
21. Dou, L.R.; Wei, X.D.; Wang, J.C.; Li, J.L.; Wang, R.C.; Zhang, S.H. Characteristics of Granitic Basement Rock Buried-Hill Reservoir in Bongor Basin, Chad. *Acta Pet. Sin.* **2015**, *36*, 898–925, (In Chinese with English abstract).
22. Guo, Z.Q.; Ma, Y.S.; Liu, W.H.; Wang, L.Q.; Tian, J.X.; Zeng, X.; Ma, F. Main Factors Controlling the Formation of Basement Hydrocarbon Reservoirs in the Qaidam Basin, Western China. *J. Pet. Sci. Eng.* **2017**, *149*, 244–255. [CrossRef]
23. Ma, F.; Yan, C.; Ma, D.; Le, X.; Huang, C.; Shi, Y.; Zhang, Y.; Xie, M. Bedrock Gas Reservoirs in Dongping Area of Qaidam Basin, NW China. *Pet. Explor. Dev.* **2015**, *42*, 293–300. [CrossRef]
24. Koning, T. Oil and Gas Production from Basement Reservoirs: Examples from Indonesia, USA and Venezuela. *Geol. Soc. Spec. Publ.* **2003**, *214*, 83–92. [CrossRef]
25. Luo, J.; Morad, S.; Liang, Z.; Zhu, Y. Controls on the Quality of Archean Metamorphic and Jurassic Volcanic Reservoir Rocks from the Xinglongtai Buried Hill, Western Depression of Liaohe Basin, China. *Am. Assoc. Pet. Geol. Bull.* **2005**, *89*, 1319–1346. [CrossRef]
26. Zou, C.N.; Hou, L.H.; Tao, S.Z.; Yuan, X.J.; Zhu, R.K.; Jia, J.H.; Zhang, X.X.; Li, F.H.; Pang, Z.L. Hydrocarbon Accumulation Mechanism and Structure of Large-Scale Volcanic Weathering Crust of the Carboniferous in Northern Xinjiang, China. *Sci. China Earth Sci.* **2012**, *55*, 221–235. [CrossRef]
27. Wu, C.; Gu, L.; Zhang, Z.; Ren, Z.; Chen, Z.; Li, W. Formation Mechanisms of Hydrocarbon Reservoirs Associated with Volcanic and Subvolcanic Intrusive Rocks: Examples in Mesozoic-Cenozoic Basins of Eastern China. *Am. Assoc. Pet. Geol. Bull.* **2006**, *90*, 137–147. [CrossRef]
28. Wang, J.; Fu, X.G.; Chen, W.X.; Wang, Z.J.; Tan, F.W.; Chen, M.; Zhuo, J.W. Chronology and Geochemistry of the Volcanic Rocks in Woruo Mountain Region, Northern Qiangtang Depression: Implications to the Late Triassic Volcanic-Sedimentary Events. *Sci. China Ser. D Earth Sci.* **2008**, *51*, 194–205. [CrossRef]

29. Fu, S.T.; Ma, D.D.; Chen, Y.; Zhang, G.Q.; Wu, K.Y. New Advance of Petroleum and Gas Exploration in Qaidam Basin. *Acta Pet. Sin.* **2016**, *37*, 1–10. (In Chinese with English abstract)
30. Jiao, X.; Niu, H.; Xie, Q.; Zhang, Y.; Li, J.; Wu, Z.; Wang, B.; Li, X. Characteristics of Basement Reservoirs and Setting for Natural Gas Accumulation in Jianbei Slope, Qaidam Basin. *Oil Gas Geol.* **2020**, *41*, 305–315. (In Chinese with English abstract) [CrossRef]
31. Lee, S.G.; de Freitas, M.H. A Revision of the Description and Classification of Weathered Granite and Its Application to Granites in Korea. *Q. J. Eng. Geol.* **1989**, *22*, 249. [CrossRef]
32. Gupta, A.S.; Rao, S.K. Weathering Indices and Their Applicability for Crystalline Rocks. *Bull. Eng. Geol. Environ.* **2001**, *60*, 201–221. [CrossRef]
33. Duzgoren-Aydin, N.S.; Aydin, A.; Malpas, J. Re-Assessment of Chemical Weathering Indices: Case Study on Pyroclastic Rocks of Hong Kong. *Eng. Geol.* **2002**, *63*, 99–119. [CrossRef]
34. Turner, B.F.; Stallard, R.F.; Brantley, S.L. Investigation of in Situ Weathering of Quartz Diorite Bedrock in the Rio Icacos Basin, Luquillo Experimental Forest, Puerto Rico. *Chem. Geol.* **2003**, *202*, 313–341. [CrossRef]
35. Shaldybin, M.V.; Wilson, M.J.; Wilson, L.; Lopushnyak, Y.M.; Kondrashova, E.S.; Rychkova, I.V.; Rudmin, M.A.; Molokov, P.B.; Muslimova, A.V. A Kaolinitic Weathering Crust in Tomsk, West Siberia: Interpretation in the Context of Weathering Crusts in Russia and Elsewhere. *Catena* **2019**, *181*, 104056. [CrossRef]
36. Fathy, D.; Wagreich, M.; Sami, M. Geochemical evidence for photic zone euxinia during greenhouse climate in the Tethys Sea, Egypt. In *Conference of the Arabian Journal of Geosciences*; Springer: Cham, Switzerland, 2022; pp. 373–374. [CrossRef]
37. Krauskopf, K.B. *Introduction to Geochemistry*, 2nd ed.; McGraw-Hill Book Co.: New York, NY, USA, 1967; p. 721.
38. Arıkan, F.; Ulusay, R.; Aydın, N. Characterization of Weathered Acidic Volcanic Rocks and a Weathering Classification Based on a Rating System. *Bull. Eng. Geol. Environ.* **2007**, *66*, 415–430. [CrossRef]
39. Ceryan, S.; Zorlu, K.; Gokceoglu, C.; Temel, A. The Use of Cation Packing Index for Characterizing the Weathering Degree of Granitic Rocks. *Eng. Geol.* **2008**, *98*, 60–74. [CrossRef]
40. Fathy, D.; Wagreich, M.; Ntaflos, T.; Sami, M. Provenance characterization of Campanian lacustrine organic-rich mudstones on the Southern Tethyan margin, Egypt. *ACS Earth Space Chem.* **2021**, *5*, 197–209. [CrossRef]
41. Von Eynatten, H.; Barceló-Vidal, C.; Pawlowsky-Glahn, V. Modelling Compositional Change: The Example of Chemical Weathering of Granitoid Rocks. *Math. Geol.* **2003**, *35*, 231–251. [CrossRef]
42. Martin, R.P.; Henchert, S.R. Principles for Description and Classification of Weathered Rock for Engineering Purposes. *Geol. Soc. Eng. Geol. Spec. Publ.* **1986**, *2*, 299–308. [CrossRef]
43. Ceryan, S.; Tudes, S.; Ceryan, N. Influence of Weathering on the Engineering Properties of Harsit Granitic Rocks (NE Turkey). *Bull. Eng. Geol. Environ.* **2008**, *67*, 97–104. [CrossRef]
44. Parker, A. An Index of Weathering for Silicate Rocks. *Geol. Mag.* **1970**, *107*, 501–504. [CrossRef]
45. Roaldset, E. Mineralogy and geochemistry of Quaternary clays in the Numedal area, southern Norway. *Nor. J. Geol.* **1972**, *52*, 335–369.
46. Nesbitt, H.W.; Young, G.M. Early Proterozoic Climates and Plate Motions Inferred from Major Element Chemistry of Lulites. *Nature* **1982**, *299*, 715–717. [CrossRef]
47. Harnois, L. The CIW Index: A New Chemical Index of Weathering. *Sediment. Geol.* **1988**, *55*, 319–322. [CrossRef]
48. Fedo, C.M.; Nesbitt, H.W.; Young, G.M. Unravelling the Effects of Potassium Metasomatism in Sedimentary Rocks and Paleosols, with Implications for Paleoweathering Conditions and Provenance. *Geology* **1995**, *23*, 921–924. [CrossRef]
49. Métivier, F.; Gaudemer, Y.; Tapponnier, P.; Meyer, B. Northeastward Growth of the Tibet Plateau Deduced from Balanced Reconstruction of Two Depositional Areas: The Qaidam and Hexi Corridor Basins, China. *Tectonics* **1998**, *17*, 823–842. [CrossRef]
50. Sobel, E.R.; Arnaud, N. A Possible Middle Paleozoic Suture in the Altyn Tagh, NW China. *Tectonics* **1999**, *18*, 64–74. [CrossRef]
51. Bian, Q.; Zhang, D.; Yu, X.; Cheng, X.; Du, W.; Liu, R.; Wang, Z.; Guo, Z. Transpressional Salt Tectonic System in Western Qaidam Basin, Western China. *AAPG Bull.* **2019**, *103*, 547–568. [CrossRef]
52. Tian, P.; Yuan, W.; Yang, X.; Feng, Z.; Chen, X.; Yuan, E. Multi-stage tectonic events of the Eastern Kunlun Mountains, Northern Tibetan Plateau constrained by fission track thermochronology. *J. Asian Earth Sci.* **2020**, *198*, 104428. [CrossRef]
53. Wu, L.; Xiao, A.; Wang, L.; Shen, Z.; Zhou, S.; Chen, Y.; Wang, L.; Liu, D.; Guan, J. Late Jurassic-Early Cretaceous Northern Qaidam Basin, NW China: Implications for the Earliest Cretaceous Intracontinental Tectonism. *Cretac. Res.* **2011**, *32*, 552–564. [CrossRef]
54. Chen, N.; Zhang, L.; Sun, M.; Wang, Q.; Kusky, T.M. U-Pb and Hf Isotopic Compositions of Detrital Zircons from the Paragneisses of the Quanji Massif, NW China: Implications for Its Early Tectonic Evolutionary History. *J. Asian Earth Sci.* **2012**, *54–55*, 110–130. [CrossRef]
55. Mattinson, C.G.; Menold, C.A.; Zhang, J.X.; Bird, D.K. High- and Ultrahigh-Pressure Metamorphism in the North Qaidam and South Altyn Terranes, Western China. *Int. Geol. Rev.* **2007**, *49*, 969–995. [CrossRef]
56. Zhang, J.; Mattinson, C.G.; Meng, F.; Wan, Y.; Tung, K. Polyphase Tectonothermal History Recorded in Granulitized Gneisses from the North Qaidam HP/UHP Metamorphic Terrane, Western China: Evidence from Zircon U-Pb Geochronology. *Bull. Geol. Soc. Am.* **2008**, *120*, 732–749. [CrossRef]
57. Wu, C.; Chen, H.; Wu, D.; Ernst, W.G. Paleozoic Granitic Magmatism and Tectonic Evolution of the South Altun Block, NW China: Constraints from Zircon U-Pb Dating and Lu-Hf Isotope Geochemistry. *J. Asian Earth Sci.* **2018**, *160*, 168–199. [CrossRef]

58. Niu, H.; Jiao, X.; Xie, Q.; Zhang, Y.; Li, X.; Wu, Z.; Wang, B.; Yang, X.; Li, Y.; Gao, Z. Origin and Tectonic Implications of Granitoids from the Eastern Segment of the South Altyn Block, North-Western China: Constraints from Petrogeochemistry, Zircon U–Pb Dating, and Lu–Hf Isotope Geochemistry. *Geol. J.* **2020**, *55*, 7613–7637. [CrossRef]
59. Cheng, F.; Jolivet, M.; Guo, Z.; Wang, L.; Zhang, C.; Li, X. Cenozoic Evolution of the Qaidam Basin and Implications for the Growth of the Northern Tibetan Plateau: A Review. *Earth-Sci. Rev.* **2021**, *220*, 103730. [CrossRef]
60. Li, W.Y. The Primary Discussion on the Relationship between Paleo-Asian Ocean and Paleo-Tethys Ocean. *Acta Petrol. Sin.* **2018**, *34*, 2201–2210, (In Chinese with English abstract).
61. Zhang, J.X.; Mattinson, C.G.; Meng, F.C.; Wan, Y.S. An Early Palaeozoic HP/HT Granulite-Garnet Peridotite Association in the South Altyn Tagh, NW China: P-T History and U-Pb Geochronology. *J. Metamorph. Geol.* **2005**, *23*, 491–510. [CrossRef]
62. Liu, L.; Wang, C.; Chen, D.; Zhang, A.; Liou, J.G. Petrology and Geochronology of HP-UHP Rocks from the South Altyn Tagh, Northwestern China. *J. Asian Earth Sci.* **2009**, *35*, 232–244. [CrossRef]
63. Wu, S.P.; Wu, C.L.; Wang, M.Y.; Chen, Q.L.; Wooden, J.L. SHRIMP U-Pb Zircon Dating of the Tula Granite Pluton on the South Side of the Altun Fault and Its Geological Implications. *Acta Geol. Sin.-Engl. Ed.* **2008**, *82*, 409–414.
64. Liu, Y.; Santosh, M.; Yuan, T.; Li, H.; Li, T. Reduction of Buried Oxidized Oceanic Crust during Subduction. *Gondwana Res.* **2016**, *32*, 11–23. [CrossRef]
65. Zhao, S.; Li, S.; Liu, X.; Santosh, M.; Somerville, I.D.; Cao, H.; Yu, S.; Zhang, Z.; Guo, L. The Northern Boundary of the Proto-Tethys Ocean: Constraints from Structural Analysis and U-Pb Zircon Geochronology of the North Qinling Terrane. *J. Asian Earth Sci.* **2015**, *113*, 560–574. [CrossRef]
66. Li, D.; He, D.; Tang, Y. Reconstructing Multiple Arc-Basin Systems in the Altai-Junggar Area (NW China): Implications for the Architecture and Evolution of the Western Central Asian Orogenic Belt. *J. Asian Earth Sci.* **2016**, *121*, 84–107. [CrossRef]
67. Zhou, F.; Zhang, Y.; Liu, Z.; Sui, G.; Li, G.; Wang, C.; Cui, S.; Zhang, Y.; Wang, J.; Zhu, J. Geochemical Characteristics and Origin of Natural Gas in the Dongping–Niudong Areas, Qaidam Basin, China. *J. Nat. Gas Geosci.* **2016**, *1*, 489–499. [CrossRef]
68. Du, W.; Chen, Y.; Wang, Z.; Bian, Q.; Guo, Z. Tectonic Analysis and Petroleum Significance of Cenozoic Faults in Dongping-Niuzhong Area in Altyn Slope. *Pet. Explor. Dev.* **2019**, *46*, 983–990. [CrossRef]
69. Plas, L.V.D.; Tobi, A.C. A Chart for Judging the Reliability of Point Counting Results. *Am. J. Sci.* **1965**, *263*, 87–90. [CrossRef]
70. Khoshbakht, F.; Memarian, H.; Mohammadnia, M. Comparison of Asmari, Pabdeh and Gurpi Formation's Fractures, Derived from Image Log. *J. Pet. Sci. Eng.* **2009**, *67*, 65–74. [CrossRef]
71. Tokhmchi, B.; Memarian, H.; Rezaee, M.R. Estimation of the Fracture Density in Fractured Zones Using Petrophysical Logs. *J. Pet. Sci. Eng.* **2010**, *72*, 206–213. [CrossRef]
72. Brekke, H.; MacEachern, J.A.; Roenitz, T.; Dashtgard, S.E. The Use of Microresistivity Image Logs for Facies Interpretations: An Example in Point-Bar Deposits of the McMurray Formation, Alberta, Canada. *AAPG Bull.* **2017**, *101*, 655–682. [CrossRef]
73. Niu, H.; Liu, S.; Lai, J.; Wang, G.; Liu, B.; Xie, Y.; Xie, W. In-Situ Stress Determination and Fracture Characterization Using Image Logs: The Paleogene Dongying Formation in Nanpu Sag, Bohai Bay Basin, China. *Energy Sci. Eng.* **2020**, *8*, 476–489. [CrossRef]
74. Clark, M.K.; Farley, K.A.; Zheng, D.; Wang, Z.; Duvall, A.R. Early Cenozoic Faulting of the Northern Tibetan Plateau Margin from Apatite (U—Th)/ He Ages. *Earth Planet. Sci. Lett.* **2010**, *296*, 78–88. [CrossRef]
75. Koryakin, A.S. Results of a Study of Proterozoic Weathering Crusts in Karelia. *Int. Geol. Rev.* **1971**, *13*, 973–980. [CrossRef]
76. Macaluso, T.; Sauro, U. Weathering Crust and Karren on Exposed Gypsum Surfaces. *Int. J. Speleol.* **1996**, *25*, 115–126. [CrossRef]
77. Wu, L.; Huang, C.; Yuan, J.; Yan, C.; Ma, F.; Sun, X. Discovery of Matrix Pore of High Efficiency in Saline Basin and Its Significance. *J. Earth Sci. Environ.* **2015**, *37*, 55–62. (In Chinese with English abstract)
78. Chen, Z.; Liu, W.; Zhang, Y.; Yan, D.; Yang, D.; Zha, M.; Li, L. Characterization of the Paleocrusts of Weathered Carboniferous Volcanics from the Junggar Basin, Western China: Significance as Gas Reservoirs. *Mar. Pet. Geol.* **2016**, *77*, 216–234. [CrossRef]
79. Ng, C.W.W.; Guan, P.; Shang, Y.J. Weathering Mechanisms and Indices of the Igneous Rocks of Hong Kong. *Q. J. Eng. Geol. Hydrogeol.* **2001**, *34*, 133–151. [CrossRef]
80. Worden, R.H.; Armitage, P.J.; Butcher, A.R.; Churchill, J.M.; Csoma, A.E.; Hollis, C.; Lander, R.H.; Omma, J.E. Petroleum Reservoir Quality Prediction: Overview and Contrasting Approaches from Sandstone and Carbonate Communities. *Geol. Soc. Spec. Publ.* **2018**, *435*, 1–31. [CrossRef]
81. Yang, W.; Wang, J.; Ma, F.; Zhang, Y.; Bai, Y.; Sun, X.; Li, H.; Zhang, J.; Wang, P. Characterization of the Weathered Basement Rocks in the Dongping Field from the Qaidam Basin, Western China: Significance as Gas Reservoirs. *Sci. Rep.* **2020**, *10*, 16694. [CrossRef]
82. George, A.D.; Marshallsea, S.J.; Wyrwoll, K.H.; Jie, C.; Yanchou, L. Miocene Cooling in the Northern Qilian Shan, Northeastern Margin of the Tibetan Plateau, Revealed by Apatite Fission-Track and Vitrinite-Reflectance Analysis. *Geology* **2001**, *29*, 939–942. [CrossRef]
83. Jolivet, M.; Brunel, M.; Seward, D.; Xu, Z.; Yang, J.; Roger, F.; Tapponnier, P.; Malavieille, J.; Arnaud, N.; Wu, C. Mesozoic and Cenozoic Tectonics of the Northern Edge of the Tibetan Plateau: Fission-Track Constraints. *Tectonophysics* **2001**, *343*, 111–134. [CrossRef]
84. Royden, L.H.; Burchfiel, B.C.; Van Der Hilst, R.D. The Geological Evolution of the Tibetan Plateau. *Science* **2008**, *321*, 1054–1058. [CrossRef] [PubMed]
85. He, P.; Song, C.; Wang, Y.; Meng, Q.; Wang, D.; Feng, Y.; Chen, L.; Feng, W. Early Cenozoic Exhumation in the Qilian Shan, Northeastern Margin of the Tibetan Plateau: Insights from Detrital Apatite Fission Track Thermochronology. *Terra Nova* **2020**, *32*, 415–424. [CrossRef]

86. Sobel, E.R. Basin Analysis of the Jurassic-Lower Cretaceous Southwest Tarim Basin, Northwest China. *Bull. Geol. Soc. Am.* **1999**, *111*, 709–724. [CrossRef]
87. Yin, A.; Rumelhart, P.E.; Butler, R.; Cowgill, E.; Harrison, T.M.; Foster, D.A.; Ingersoll, R.V.; Zhang, Q.; Zhou, X.Q.; Wang, X.F.; et al. Tectonic History of the Altyn Tagh Fault System in Northern Tibet Inferred from Cenozoic Sedimentation. *Bull. Geol. Soc. Am.* **2002**, *114*, 1257–1295. [CrossRef]
88. Sun, G.Q.; Liu, W.M.; Guo, J.J.; Wang, Y.T. Fission-Track Evidence of Tectonic Evolution in the Northwestern Qaidam Basin, China. *J. Earth Syst. Sci.* **2018**, *127*, 12. [CrossRef]
89. Tang, L.; Jin, Z.; Zhang, M.; Liu, C.; Wu, H.; You, F.; Zhang, B. An Analysis on Tectono-Paleogeography of the Qaidam Basin, NW China. *Earth Sci. Front.* **2000**, *7*, 421–429. (In Chinese with English abstract)
90. Matte, P.; Tapponnier, P.; Arnaud, N.; Bourjot, L.; Avouac, J.P.; Vidal, P.; Qing, L.; Yusheng, P.; Yi, W. Tectonics of Western Tibet, between the Tarim and the Indus. *Earth Planet. Sci. Lett.* **1996**, *142*, 311–330. [CrossRef]
91. Metcalfe, I. Multiple Tethyan Ocean Basins and Orogenic Belts in Asia. *Gondwana Res.* **2021**, *100*, 87–130. [CrossRef]
92. Liu, Y.; Ye, H.; Ge, X.; Chen, W.; Liu, J.; Ren, S.; Pan, H. Laser Probe $^{40}Ar/^{39}Ar$ Dating of Mica on the Deformed Rocks from Altyn Fault and Its Tectonic Implications, Western China. *Chin. Sci. Bull.* **2001**, *46*, 322–325. [CrossRef]
93. Zheng, D.; Clark, M.K.; Zhang, P.; Zheng, W.; Farley, K.A. Erosion, Fault Initiation and Topographic Growth of the North Qilian Shan (Northern Tibetan Plateau). *Geosphere* **2010**, *6*, 937–941. [CrossRef]
94. Qi, B.; Hu, D.; Yang, X.; Zhang, Y.; Tan, C.; Zhang, P.; Feng, C. Apatite Fission Track Evidence for the Cretaceous-Cenozoic Cooling History of the Qilian Shan (NW China) and for Stepwise Northeastward Growth of the Northeastern Tibetan Plateau since Early Eocene. *J. Asian Earth Sci.* **2016**, *124*, 28–41. [CrossRef]
95. Yu, J.; Zheng, D.; Pang, J.; Wang, Y.; Fox, M.; Vermeesch, P.; Li, C.; Xiao, L.; Hao, Y.; Wang, Y. Miocene Range Growth Along the Altyn Tagh Fault: Insights From Apatite Fission Track and (U-Th)/He Thermochronometry in the Western Danghenan Shan, China. *J. Geophys. Res. Solid Earth* **2019**, *124*, 9433–9453. [CrossRef]
96. Chen, Z.L.; Gong, H.L.; Li, L.; Wang, X.F.; Chen, B.L.; Chen, X. Cenozoic Uplifting and Exhumation Process of the Altyn Tagh Mountains. *Earth Sci. Front.* **2006**, *13*, 92–102. (In Chinese with English abstract)
97. Sun, Y.; Chen, Z.L.; Chen, B.L.; Han, F.B.; Zhou, Y.G.; Hao, R.X.; Li, S.B. Cenozoic Uplift and Denudation of the EW-Trending Range of Northern Altun Mountains: Evidence from Apatite Fission Track Data. *Acta Geosci. Sin.* **2014**, *35*, 67–75, (In Chinese with English abstract). [CrossRef]
98. Wan, J.L.; Wang, Y.; Li, Q.; Wang, F.; Wang, E. FT Evidence of Northern Altyn Uplift in Late Cenozoic. *Bull. Mineral. Petrol. Geochem.* **2001**, *20*, 222–224. (In Chinese with English abstract)
99. Wang, E.; Xu, F.Y.; Zhou, J.X.; Wan, J.; Burchfiel, B.C. Eastward Migration of the Qaidam Basin and Its Implications for Cenozoic Evolution of the Altyn Tagh Fault and Associated River Systems. *Bull. Geol. Soc. Am.* **2006**, *118*, 349–365. [CrossRef]
100. Wang, Y.; Zheng, J.; Zheng, Y.; Liu, X.; Sun, G. Paleocene-Early Eocene Uplift of the Altyn Tagh Mountain: Evidence from Detrital Zircon Fission Track Analysis and Seismic Sections in the Northwestern Qaidam Basin. *J. Geophys. Res. Solid Earth* **2015**, *120*, 8534–8550. [CrossRef]
101. Peng, Y.H. Apatite Fission Track Ages and Significance of Northern Qaidam Basin. Master's Thesis, Lanzhou University, Lanzhou, China, 2009. (In Chinese with English abstract)
102. Meng, Q.R.; Hu, J.M.; Yang, F.Z. Timing and Magnitude of Displacement on the Altyn Tagh Fault: Constraints from Stratigraphic Correlation of Adjoining Tarim and Qaidam Basins, NW China. *Terra Nova* **2001**, *13*, 86–91. [CrossRef]
103. Wu, L.; Xiao, A.; Yang, S.; Wang, L.; Mao, L.; Wang, L.; Dong, Y.; Xu, B. Two-Stage Evolution of the Altyn Tagh Fault during the Cenozoic: New Insight from Provenance Analysis of a Geological Section in NW Qaidam Basin, NW China. *Terra Nova* **2012**, *24*, 387–395. [CrossRef]